EUROPEAN ORGANIZATION FOR NUCLEAR RESEARCH
CERN — ACCELERATORS AND TECHNOLOGY SECTOR

CERN–ACC–2015–0015
22 January 2015

ION COLLIDERS

Wolfram Fischer
Brookhaven National Laboratory, Upton, New York 11973, USA.

John M. Jowett
CERN, CH-1211 Geneva 23, Switzerland.

Abstract

High-energy ion colliders are large research tools in nuclear physics to study the Quark-Gluon-Plasma (QGP). The range of collision energy and high luminosity are important design and operational considerations. The experiments also expect flexibility with frequent changes in the collision energy, detector fields, and ion species. Ion species range from protons, including polarized protons in RHIC, to heavy nuclei like gold, lead and uranium. Asymmetric collision combinations (e.g. protons against heavy ions) are also essential. For the creation, acceleration, and storage of bright intense ion beams, limits are set by space charge, charge change, and intrabeam scattering effects, as well as beam losses due to a variety of other phenomena. Currently, there are two operating ion colliders, the Relativistic Heavy Ion Collider (RHIC) at BNL, and the Large Hadron Collider (LHC) at CERN.

Invited Contribution to Reviews of Accelerator Science & Technology, Vol. 7 (2014), Editors Alexander W. Chao and Weiren Chou, World Scientific Pub., Singapore

CONTENTS

LIST OF FIGURES

LIST OF TABLES

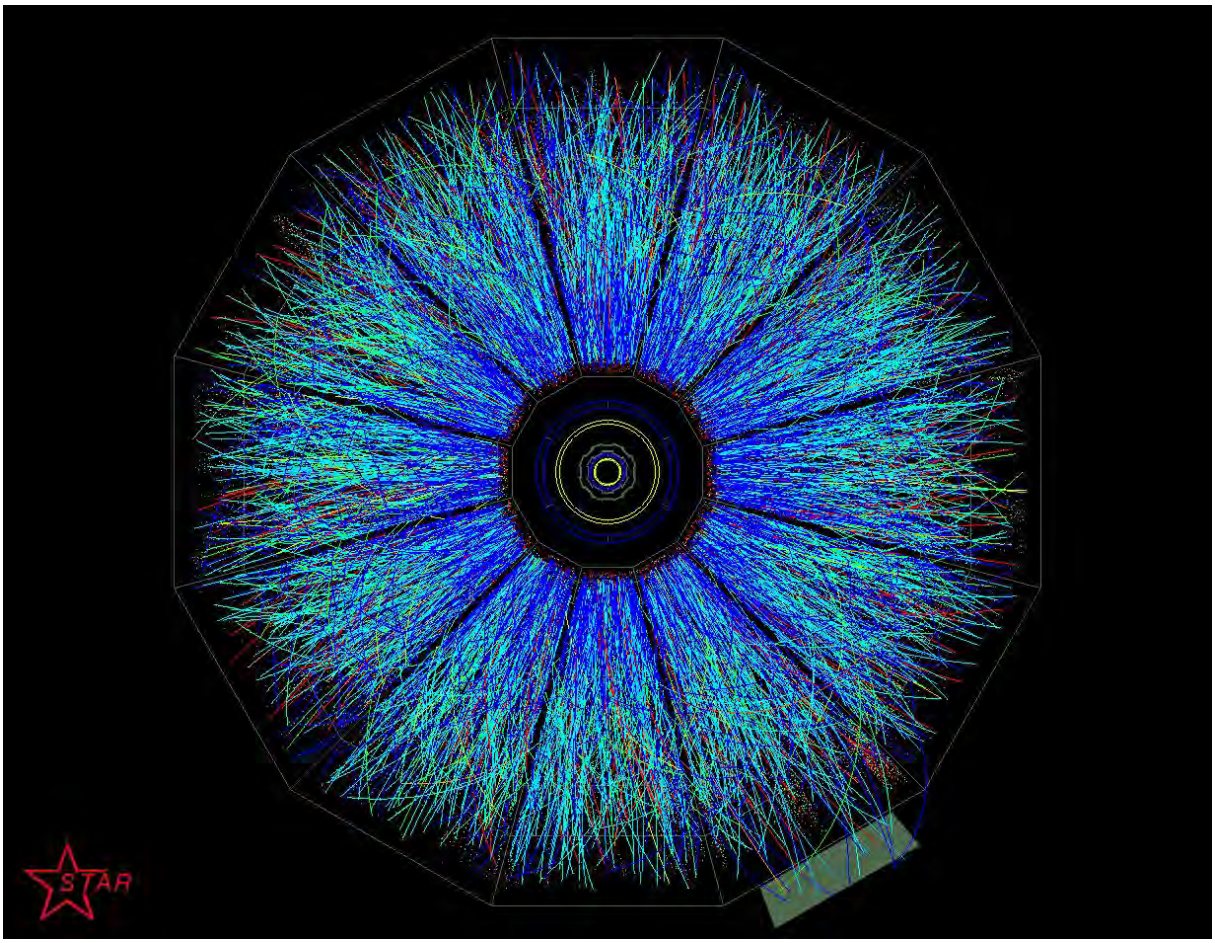

Fig. 1: Au+Au event display in the STAR detector at RHIC (courtesy STAR collaboration).

1 INTRODUCTION

To date three ion colliders have been built and operated (Table 1). The Intersecting Storage Rings (ISR) [1] at CERN were not only the first p+p and p+$\bar{\text{p}}$ collider (1973-1983) but also very briefly collided light ions beginning in 1977 [2, 3]. The Relativistic Heavy Ion Collider (RHIC) [4] at BNL started operation in 2000, and is expected to run for more than two decades. The Large Hadron Collider (LHC) [6–9] at CERN had first heavy-ion collisions in 2010, and is also expected to operate for more than two decades. In this review we shall discuss primarily the present generation of ion colliders comprising RHIC and the LHC with just a brief look beyond. While RHIC operation is dedicated to the physics of heavy ion collisions and the spin of nucleons, the LHC operates as an ion collider for about one month in each operating year; its operation as a proton-proton collider for elementary particle physics is discussed elsewhere. However, in both colliders, certain proton runs are specifically designed to provide reference data to compare with the heavy-ion collisions. The main parameters for Au beams in RHIC and Pb beams in the LHC are shown in Table 2.

High energy ion colliders are large research tools to study the interactions of quarks and gluons. These interactions are described by the theory of Quantum Chromo Dynamics (QCD). The collisions of high-energy ions create matter of colossal temperature and density that existed only microseconds after the Big Bang, and thousands of secondary particles can be generated in the collisions (Fig. 1). The much higher center of mass energy available at colliders enables

Table 1: Ion combinations in long and short notation†, and center-of-mass energy ranges per nucleon-pair $\sqrt{s_{\rm NN}}$ for ISR [1–3], RHIC [5], and LHC [6]. The symbol ↑ in the short notation indicates spin polarized beams. Planned extensions are given in square brackets.

species combination		nucleon-pair center-of-mass energy $\sqrt{s_{\rm NN}}$ (GeV)		
		ISR	RHIC	LHC
$^{1}H^{1+}$ + $^{1}H^{1+}$	p+p	17 – 62.4	—	900 – 8000 [14000]
$^{1}H^{1+}$ + $^{1}H^{1+}$	p↑+p↑	—	31.2 – 510	—
$^{1}H^{1+}$ + $^{1}\bar{H}^{1+}$	p+$\bar{\rm p}$	30 – 62.4	—	—
$^{1}H^{1+}$ + $^{2}H^{1+}$	p+d	37.6 – 44.4	—	—
$^{1}H^{1+}$ + $^{3}He^{2+}$	p↑+h↑	—	[200]	—
$^{1}H^{1+}$ + $^{4}He^{2+}$	p+α	37.6 – 44.4	—	—
$^{1}H^{1+}$ + $^{27}Al^{13+}$	p↑+Al	—	[200]	—
$^{1}H^{1+}$ + $^{197}Au^{79+}$	p↑+Au	—	[200]	—
$^{1}H^{1+}$ + $^{208}Pb^{82+}$	p+Pb	—	—	5023 [8790]
$^{2}H^{1+}$ + $^{2}H^{1+}$	d+d	26.6 – 31.4	—	—
$^{2}H^{1+}$ + $^{197}Au^{79+}$	d+Au	—	200	—
$^{3}He^{2+}$ + $^{197}Au^{79+}$	h+Au	—	200	—
$^{4}He^{2+}$ + $^{4}He^{2+}$	α+α	26.6 – 31.4	—	—
$^{40}Ar^{18+}$ + $^{40}Ar^{18+}$	Ar+Ar	—	—	[6300]
$^{63}Cu^{29+}$ + $^{63}Cu^{29+}$	Cu+Cu	—	22.4 – 200	—
$^{63}Cu^{29+}$ + $^{197}Au^{79+}$	Cu+Au	—	200	—
$^{197}Au^{79+}$ + $^{197}Au^{79+}$	Au+Au	—	[5.0] 7.7 – 200	—
$^{208}Pb^{82+}$ + $^{208}Pb^{82+}$	Pb+Pb	—	—	2760 – 3153 [5518]
$^{235}U^{92+}$ + $^{235}U^{92+}$	U+U	—	192.8	—

† p or $^{1}H^{1+}$ (proton) is the nucleus of the ^{1}H atom (hydrogen); $\bar{\rm p}$ (p-bar or anti-proton) is the anti-particle to p (proton); d or $^{2}H^{1+}$ (deuteron) is the nucleus of the ^{2}H atom (deuterium); h or $^{3}He^{2+}$ (helion) is the nucleus of the ^{3}He atom (helium-3); α or $^{4}He^{2+}$ (alpha) is the nucleus of the ^{4}He atom (helium-4).

them to explore regions of the nuclear matter phase diagram (as function of temperature and baryon density) that are inaccessible to complementary fixed target experiments, although at much lower luminosities than these.

The creation of a new form of matter — the Quark-Gluon-Plasma (QGP) — was expected at a temperature of 2 trillion kelvin (equivalent to an energy of 150 MeV). Experiments at RHIC have confirmed the existence of this form of matter, although they discovered it with properties different from expectations [10]. The QGP was anticipated to be a weakly interacting gas-like medium of quarks and gluons, but found to be strongly interacting like an almost perfect liquid. It is the substance closest to a perfect liquid known to date [11]. The QGP also has a remarkably short mean free path for penetrating probes, leading to a phenomenon called "jet quenching" where a jet is suppressed (while its recoil jet may exit the QGP) [10]. The collision of high-energy ions also create the heaviest man-made anti-matter nuclei such as the anti-hypertriton ($^{3}_{\Lambda}\overline{\rm H}$) [12] and anti-helium-4 nucleus ($^{4}\overline{\rm He}$) [13].

Experiments with colliding ion beams aim to explore the largest possible region of the nuclear matter phase diagram (temperature vs. density) from the lowest to the highest temperatures, corresponding to the lowest and highest collision energies, and different geometries with collisions of light on light ions, light on heavy ions, and heavy on heavy ions. The energy range,

luminosity and flexibility in selecting and changing the collision energy and species are the major design considerations for ion colliders. Recently the RHIC energy range was even extended below the nominal injection energy, in search of a critical point in the nuclear matter phase diagram [14]. With RHIC and the LHC combined, a large energy range can be spanned, thus creating QGP with a wide range of initial temperatures. Table 1 lists all species combinations and energies that the three ion colliders ISR, RHIC and LHC have operated with, and presently planned extensions to the species combinations and energies.

RHIC started with four experiments: the large detectors STAR and PHENIX, and the smaller detectors PHOBOS and BRAHMS. STAR is specialized in recording the tracks of the individual particles generated in ion-ion collisions (Fig. 1) while PHENIX is optimized to detect electromagnetic probes (photons and leptons) that are not affected by the strong force. The PHOBOS experiment was built so that large numbers of unbiased collision events could be analyzed for unusual signatures. BRAHMS, which included a forward spectrometer, was designed to measure charged hadrons over a wide rapidity range. PHOBOS completed data taking in 2005 and BRAHMS in 2006 [16].

The LHC has now completed its first four years (known as "Run 1") of ion operation and is being prepared for an additional step in energy in 2015. The initial step for a factor 14 in energy, $\sqrt{s_{\rm NN}}$, from RHIC to LHC was the largest for collisions of a similar type (Au+Au and Pb+Pb) in the history of particle accelerators. An even greater step was realized in 2012 in the asymmetric p+Pb collisions. The LHC provides collisions to a new generation of highly capable detectors in a wide range of collision conditions [17, 18]. ALICE is specifically designed for heavy ion collisions with a large Time-Projection Chamber (TPC) to study the high multiplicity heavy-ion collisions in great detail and also features a large forward muon spectrometer arm and electromagnetic calorimeter. These features give it an unparalleled capacity to extract precise physical observables from the plethora of tracks visible in typical collision events [19].

The large general purpose LHC detectors ATLAS and CMS have complementary capabilities for the study of heavy-ion collisions and also participate fully in the heavy-ion program of the LHC. In the p+Pb runs, the capabilities of the fourth large, asymmetric, detector LHCb were brought to bear. The smaller forward detectors, TOTEM and ALFA, worked together with CMS and ATLAS to extend their rapidity coverage and the LHCf detector took data relevant to the understanding of the interactions of the highest energy cosmic rays with the Earth's atmosphere.

The higher energies at the LHC have confirmed many of the RHIC results on the fluid properties of the QGP but also created many more rare "hard probes" of the hot medium. These include spectacularly visible jets, groups of high-$p_\perp$ particles emitted within narrow cones, and bound states of heavy quark-anti-quark pairs such as charmonium (J/ψ) or bottomonium (Υ). There are new measurements of jet-quenching [20–22]. The Debye-like screening of the color force [19, 23] between quark and anti-quark pairs by the hot medium manifests itself in the "melting" of these massive states [19, 23]. The energy of the collisions is so high that massive particles such as Z and W bosons, never before seen in heavy-ion collisions, can be created and easily identified (Fig. 2). Together with prompt photons, these are hard probes that do not couple to the QGP via the strong interaction. The ALICE experiment [19, 24] has reported the highest temperature measured directly in the laboratory from the photon spectrum emitted by the QGP [25], and the study of the hydrodynamic flow properties of the QGP has been taken to new levels with detailed study of the effect of initial state fluctuations. At the other extreme of multiplicity it has also yielded results on the production of the J/ψ in ultraperipheral collisions where only the intense photon fields of the nuclei interact and a single pair of tracks appear in an otherwise empty detector. Like STAR, it has also identified a range of heavy anti-matter and

Table 2: Main parameters for Au beams in RHIC [5], and Pb beams in the LHC [6, 15].

parameter	unit	RHIC (Au)			LHC (Pb)		
		design 2000†	achieved 2014	upgrade ≥2016	design 2009†	achieved 2011	upgrade ≥2018
circumference C	km		— 3.834 —			— 26.659 —	
mass and charge numbers A, Z	...		— 197, 79 —			— 208, 82 —	
maximum beam energy E	GeV/nucleon		— 100 —		2759	1380*	2759
bunch intensity N_b	10^9	1.0	1.6	2.0	0.07	0.12	0.22
number of bunches k_b	...	60	111	111	592	358	912
normalized rms emittance, initial ϵ_N	μm		— 2.5 —			— 1.5 —	
rms bunch length σ_s, initial	m		— 0.3 —		0.08	0.11	0.10
beam-beam parameter ξ/IP	10^{-3}	2.3	2.5	2.9	0.20	0.35	0.64
stored beam energy	MJ/beam	0.12	0.56	0.70	3.8	2.3	18
peak and avg. store luminosities $\mathcal{L}_{peak}/\mathcal{L}_{avg}$	$10^{26}\text{cm}^{-2}\text{s}^{-1}$	8/2	84/50	125/100	10/7	5/3	60/40
nucleon-pair luminosities $\mathcal{L}_{NN,peak}/\mathcal{L}_{NN,avg}$	$10^{30}\text{cm}^{-2}\text{s}^{-1}$	31/8	326/194	485/388	43/30	22/13	260/173

† First year of operation.

* Pb and p beams reached 1577 and 4000 GeV/nucleon in 2012.

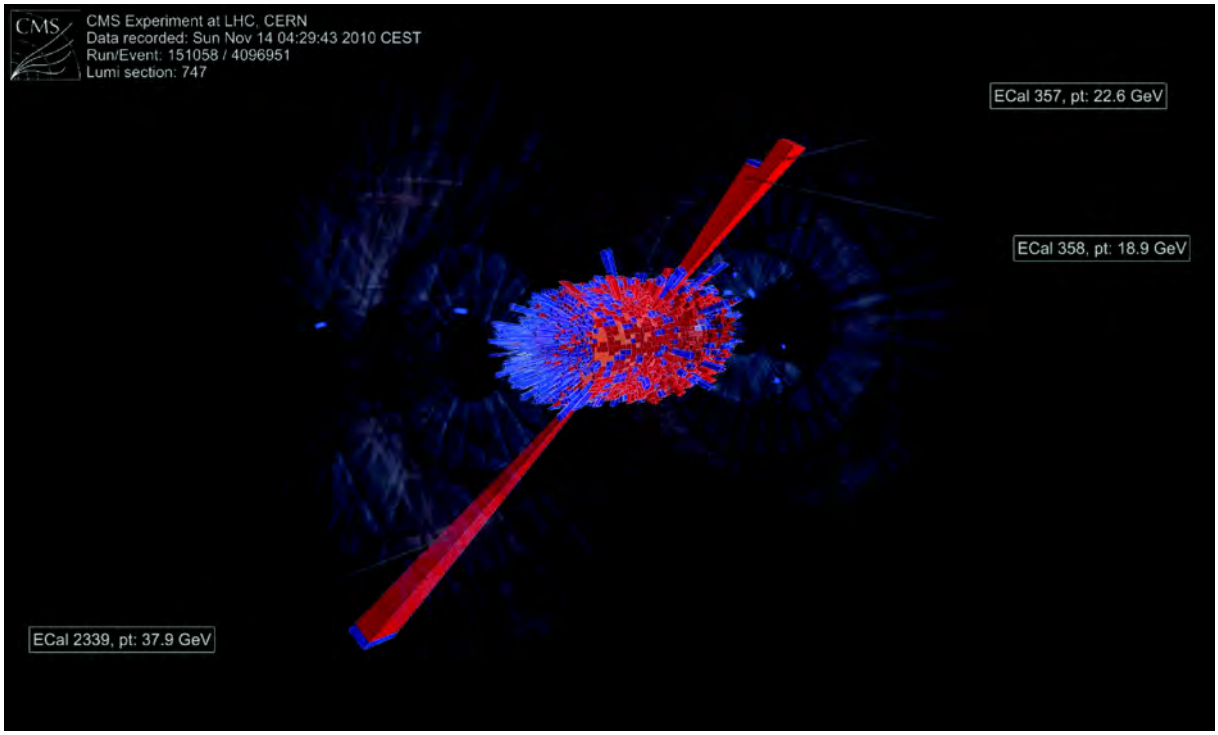

Fig. 2: Pb+Pb event display in the CMS detector at LHC showing the decay of a Z boson (CMS-PHO-EVENTS-2010-004-1).

hyper-matter nuclei created in Pb+Pb collisions [26].

As in RHIC, a large part of the motivation for proton-proton and proton-nucleus collisions at the LHC [27] was initially to provide reference data to define the cold-nuclear matter effects and better analyze the nucleus-nucleus collisions. A further motivation was the study of low-x physics and the investigation of the possible existence of the color-glass condensate. However some quite unexpected phenomena have also been observed, starting with the single pilot p+Pb fill in 2012. The ALICE experiment [28] showed that the nuclear modification factor $R_{\rm pPb}$ is consistent with unity for p_T above $2\,\mathrm{GeV}/c$. This measurement, shown in Fig. 4, indicates that the strong suppression of hadron production at high p_T observed in Pb+Pb collisions at the LHC is not due to an initial-state effect.

Another striking observation is the emergence of long-range correlations originally seen in very rare high-multiplicity p+p collisions by the CMS experiment in 2010 [29]. Similar effects were found [30] with a much greater, and totally unexpected, strength in p+Pb collisions. Indeed the effect is of comparable strength to Pb+Pb collisions where it was expected. Although there is as yet no general consensus as to their interpretation, they strongly suggest that collective behavior, perhaps tiny droplets of QGP, may emerge even on the scale of the proton radius.

In addition to being a versatile high-luminosity ion collider, RHIC is also the world's first and only collider of spin-polarized protons [31]. The collisions of polarized protons are used to unravel the origin of the proton spin. Even with the newest experimental results, only 30% of the proton spin is found to be from the quarks inside the proton (measured for momentum fraction $x > 0.001$) [32], and the inability to explain the origin of the proton spin had been termed the "proton spin crisis". The remaining contributions to the spin are either from the gluons or the orbital angular momentum of the gluons. The most recent results show that the gluons themselves contribute 10% to the spin in the still limited momentum range of $0.05 < x < 0.2$ [32, 33].

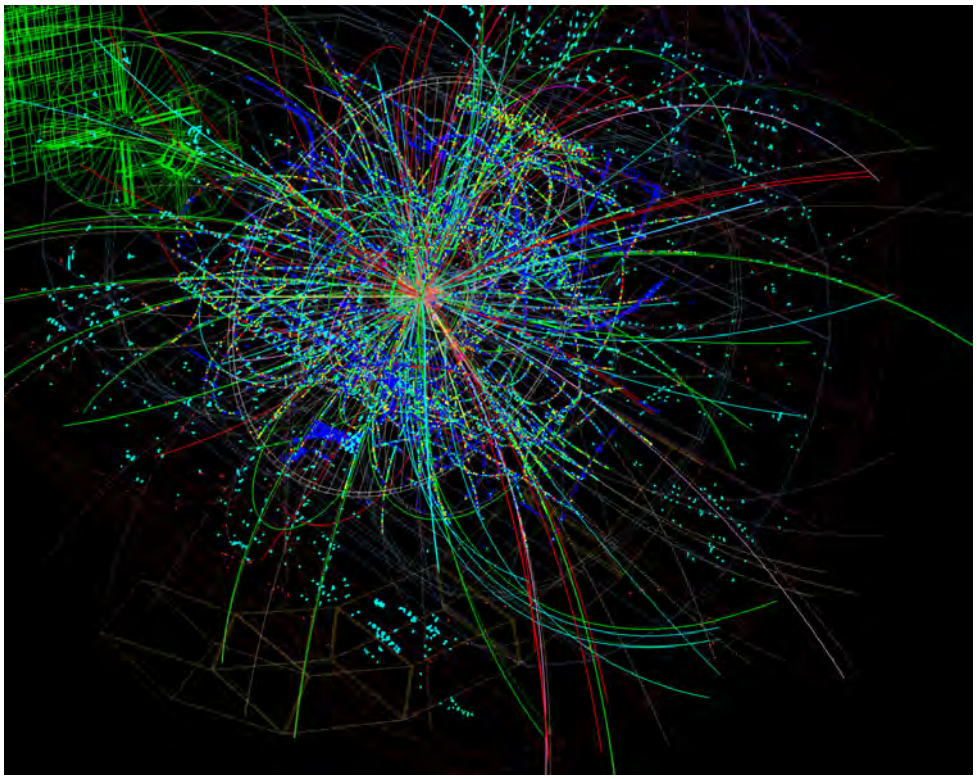

Fig. 3: A proton-lead nucleus collision measured in ALICE during the pilot run at LHC 13.9.2012 (ALICE-PHO-GEN-2012-007-19).

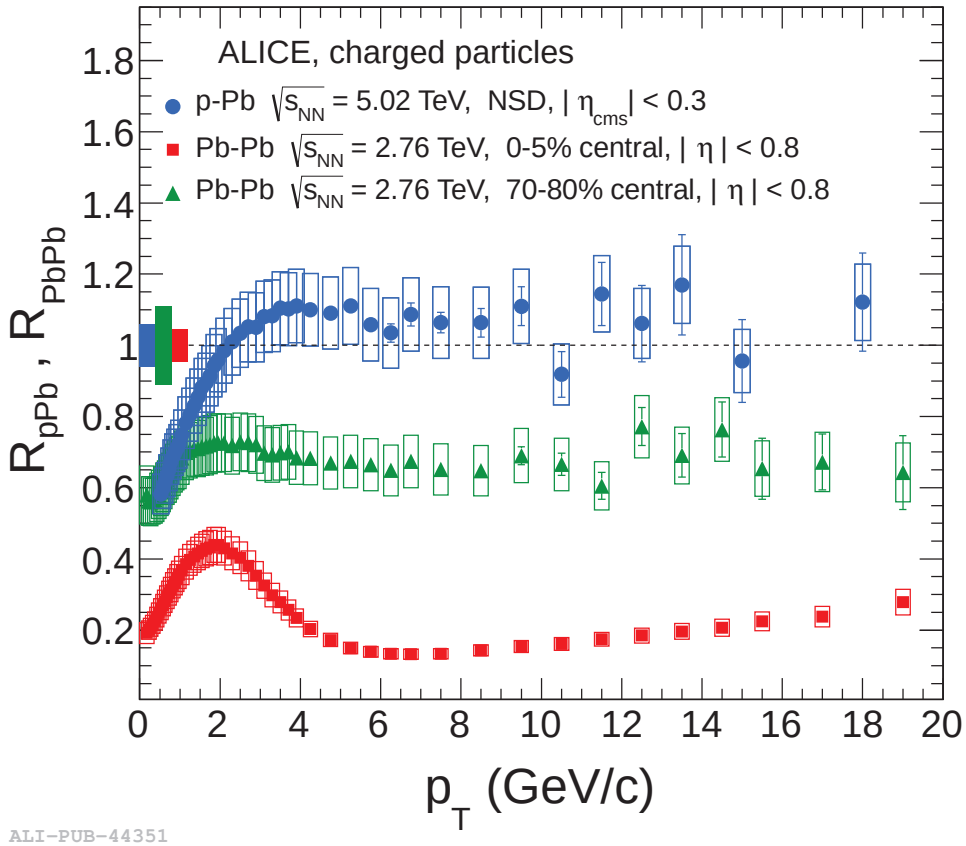

Fig. 4: Nuclear modification factor measured by ALICE from the first p+Pb pilot fill [28].

The collisions of high-energy polarized protons give experimental data complementary to deep inelastic scattering experiments with electron beams. In the future, collisions with polarized neutrons are also planned. These come in the form of polarized ^{3}He.

2 ENERGY AND LUMINOSITY

For physics purposes, the collisions are characterized by the average center-of-mass energy of colliding nucleon pairs within the colliding nuclei. If the latter have charges Z_1, Z_2, nucleon numbers A_1, A_2 and the magnetic field in the two rings is set for protons of energy $E_p \gg m_p c^2$, then this energy parameter is

$$\sqrt{s_{\rm NN}} \approx 2\, E_p \sqrt{\frac{Z_1 Z_2}{A_1 A_2}} \tag{1}$$

For asymmetric collisions, the experiments must contend with a corresponding central rapidity shift

$$y_{\rm NN} \approx \frac{1}{2} \log\left(\frac{Z_1 A_2}{A_1 Z_2}\right). \tag{2}$$

These relations apply strictly when the magnetic fields of the two rings are equal, as imposed by the "two-in-one" magnet design of the LHC. RHIC has two separate rings and the magnetic fields may be chosen differently (see Section 4.1).

We recall the luminosity formula since much of the ion beam preparation (Sec. 3), collider operation (Sections 4 and 5) and the upgrades (Sec. 7) are aimed at maximizing this quantity. Descriptions of the specific ion luminosity limits in RHIC and the LHC are given in Section 5. The time-dependent luminosity at a given interaction point (IP) is given by [34]

$$\mathcal{L}(t) = (\beta\gamma)\frac{f_{\rm rev}}{4\pi} k_c \frac{N_{b1}(t) N_{b2}(t)}{\epsilon_n(t)\beta^*(t)} h(\sigma_s(t), \theta(t)) \tag{3}$$

where $(\beta\gamma)$ are the relativistic factors, $f_{\rm rev}$ is the revolution frequency, k_c is the number of bunch pairs colliding at the IP ($k_c \leq k_b$ the total number of bunches in either beam), N_{b1} and N_{b2} the bunch intensities for the two beams respectively, ϵ_n the normalized rms emittance, and β^* the lattice function at the interaction point. The factor h is of order and smaller than one and captures the geometric luminosity reduction due to the hourglass effect with bunch length σ_s, and a crossing angle θ [34]. In Eq. (3) it is assumed that all bunches in a ring have the same intensity N_b, and that the transverse emittances and lattice functions at the interaction point are the same for both planes and both rings. With equal ion species we have $\mathcal{L} \propto N_b^2$, and typically the largest gains in luminosity can be made through an increase in the bunch intensity N_b. When these assumptions do not hold (e.g., in the LHC, Fig. 10) one has to sum over the parameters of colliding bunch pairs [35].

To compare the luminosities for different species (Table 2, Figs. 5 and 6) the nucleon-pair luminosity is the physically relevant quantity, just as $\sqrt{s_{\rm NN}}$ is the relevant collision energy:

$$\mathcal{L}_{\rm NN} = A_1 A_2 \mathcal{L}. \tag{4}$$

For the nucleon-pair luminosity the beams are thought of as being made of nucleons rather than ions. We denote the time-integrated luminosities by

$$L = \int \mathcal{L}(t) dt \quad \text{and} \quad L_{\rm NN} = \int \mathcal{L}_{\rm NN}(t) dt. \tag{5}$$

Figure 5 shows the integrated nucleon-pair luminosity delivered to one of the RHIC experiments over all RHIC runs and species combinations (except p+p) to date. Figure 6 shows similar data for all the LHC experiments. Note the different scales and that the annual LHC heavy-ion runs are shorter and, so far, fewer than those of RHIC. Also note that, for example, the LHC p+Pb run in 2013 provided an $L_{\rm NN}$ well-matched, as reference data, to that of the previous Pb+Pb runs (although $\sqrt{s_{\rm NN}}$ was higher).

3 ION BEAM PREPARATION

For collider operation ion bunches of sufficient intensity N_b and small enough emittances $\epsilon_{x,y,s}$ are needed to satisfy the experimental luminosity requirements. In the preparation of ion beams, a number of effects pose limits to the achievable intensity and emittance. These include space charge, intrabeam scattering (IBS), charge change processes, and dynamic vacuum pressure rise through ion impact desorption after beam loss.

Although a high charge state Z allows for more efficient acceleration (the energy gain from an accelerating voltage V is $\Delta E = ZeV$), at low energies the charge state is kept low to reduce the effects of space charge, intrabeam scattering, and electron capture. The charge state is progressively increased in the accelerator chain (Table 3).

3.0.1 Space charge.

The direct space charge tune shift of an ion without the effect of the beam pipe is [36]

$$\Delta Q = -\frac{\lambda R}{2\epsilon_n \beta\gamma^2}\frac{r_0 Z^2}{A} \tag{6}$$

where λ is the particle line density, R the accelerator radius, and r_0 is the classical proton radius. The beam pipe also modifies the tune, with terms proportional to $1/\gamma$ and depending on the beam pipe geometry and material. These terms need to be added to right hand side of Eq. (6). In fast ramping accelerators the tolerable tune spread ΔQ is typically limited to less than 0.5. To minimize ΔQ the charge state Z is kept low at small γ values, and γ is increased as fast as possible through rapid acceleration.

3.0.2 Intrabeam scattering.

The emittance growth rates due to intrabeam scattering can be written as [37]

$$\frac{d}{dt}\begin{pmatrix}\epsilon_x\\ \epsilon_y\\ \epsilon_s\end{pmatrix} = \frac{N_b c}{\gamma\epsilon_x\epsilon_y\epsilon_s}\frac{r_0^2 Z^4}{A^2}\begin{pmatrix}F_x\\ F_y\\ F_s\end{pmatrix} \tag{7}$$

where the functions $F_{x,y,s}$ are functions of the lattice parameters and beam sizes averaged over the machine circumference (the $F_{x,y,s}$ also have some γ dependence) [37]. Intrabeam scattering is particularly strong for ions with high charge states Z. For heavy ions at the end of the RHIC accelerator chain the factor $N_b Z^4/A^2$ is typically an order of magnitude larger than that for protons. As with space charge, a low charge state Z is preferred at low energies to minimize intrabeam scattering effects.

3.0.3 Charge change processes.

Interaction of the ions with the residual gas can change the charge state Z through either electron capture or electron loss [38, 39]. The cross sections of the processes change with energy, and,

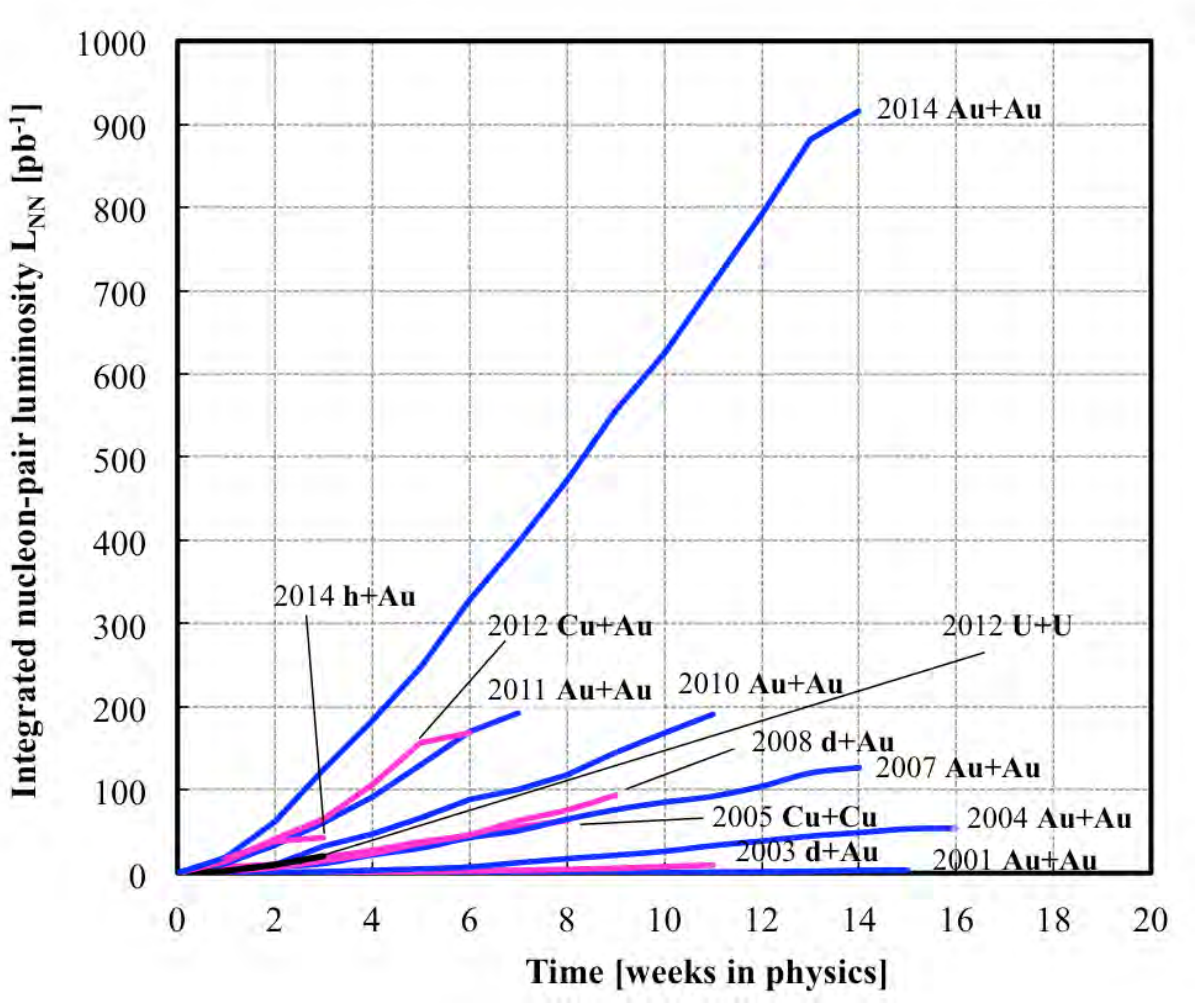

Fig. 5: Integrated nucleon-pair luminosity L_{NN} delivered to PHENIX, one of the two high-luminosity experiments at RHIC from 2000 to 2014. The luminosity for 2000 is too small to be visible [5].

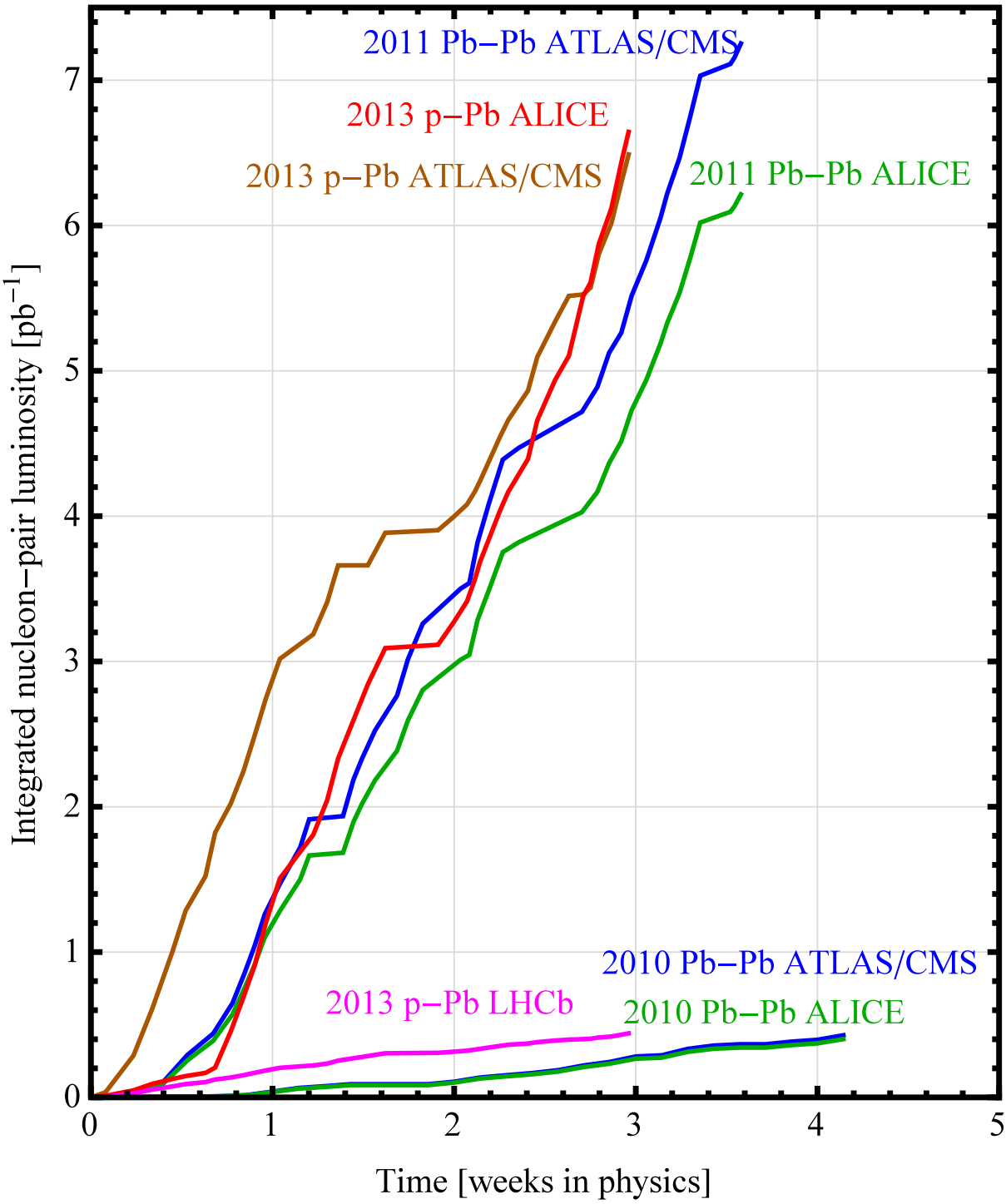

Fig. 6: Integrated nucleon-pair luminosity L_{NN} delivered to the three high-luminosity experiments ALICE, ATLAS and CMS during Run 1 (2010, 2011 and 2013) of the LHC. The lower level of luminosity taken by the LHCb experiment during the 2013 p+Pb run is also shown. Data from the single pilot p+Pb fill in 2012 are not shown.

Table 3: Preparation of Au beams for RHIC and Pb beams for the LHC. For each accelerator the kinetic energy is given at extraction, the charge state is in the following transfer line [41,42].

RHIC, achieved 2014 (Au)				LHC, achieved 2011 (Pb)			
machine	ion charge state Z	kinetic energy [eV/nucleon]	intensity per RHIC bunch [10^9]	machine	ion charge state Z	kinetic energy [eV/nucleon]	intensity per LHC bunch [10^9]
EBIS	32+	8.5 k	5.1	ECR	27+	2.5 k	8.6
RFQ/LINAC	32+	2.0 M	4.5	RFQ/LINAC3	54+	4.2 M	0.57
Booster	77+	101 M	4.0	LEIR	54+	72.2 M	0.55
AGS	79+	8.8 G	2.1	PS	82+	5.9 G	0.38
RHIC	79+	99 G	1.6	SPS	82+	177 G	0.22
				LHC	82+	1.58 T	0.2

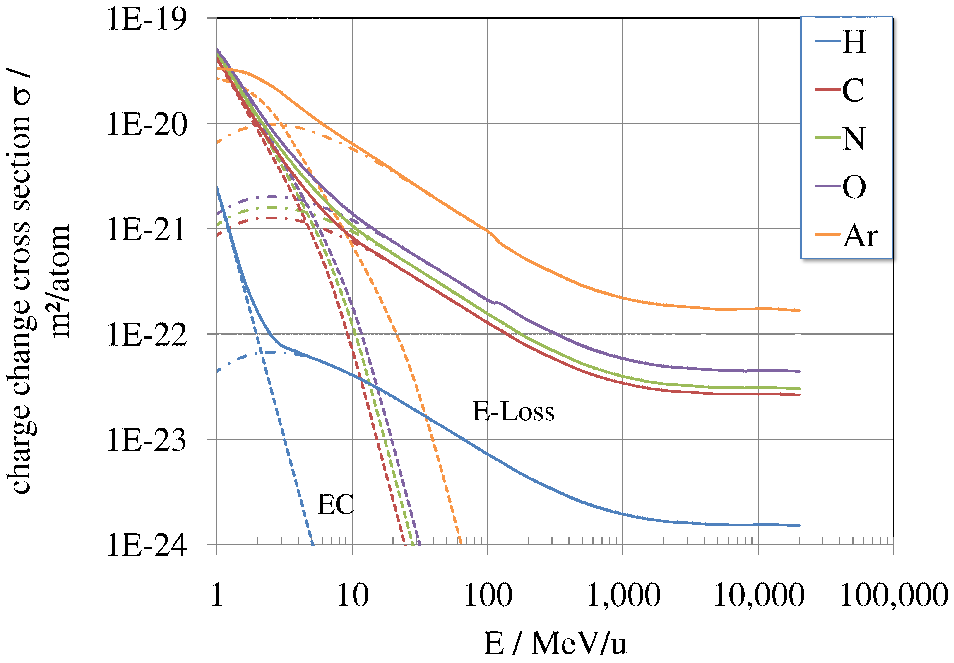

Fig. 7: Calculated charge change cross sections for Au^{31+} for various target atoms [40]. EC denotes electron capture and E-loss denotes electron stripping cross sections.

as an example, Fig. 7 shows the calculated electron capture and electron loss cross sections for Au^{31+} as a function of energy for a number of target atoms. In Fig. 7 the capture cross sections fall rapidly with an increase in the beam energy, stripping cross sections also fall but at a slower rate until they level off.

3.0.4 Dynamic vacuum pressure rise.

The loss of ions on the beam pipe wall can release gas molecules, which in turn leads to larger beam losses. Because of this mechanism an increased input intensity could result in a lower output intensity.

Measured desorption yields $\eta_{ionloss}$ (gas molecules released per lost ion) vary widely and some measurements show values higher than 10^5 [43]. The ion-impact desorption yield is dependent on the ion energy and impact angle (with higher $\eta_{ionloss}$ values for grazing angles), and the surface properties of the beam pipe wall (with large $\eta_{ionloss}$ values for surfaces with many mono-layers of adsorbed gas).

A dynamic gas load can also be created when ionized residual gas molecules are accelerated in the electromagnetic field of the beam (η_{ion}), and when the electrons of an electron cloud [44] hit the beam pipe (η_e). The dynamic pressure from these effects is [45]

$$P = \frac{Q_0 + kTL\left(\frac{1}{e}\frac{dI_e}{dl}\eta_e + \frac{d^2N_{\mathrm{tot}}}{dldt}\eta_{\mathrm{ionloss}}\right)}{S - \eta_{\mathrm{ion}}Lb} \tag{8}$$

where Q_0 is the static gas load, P is the pressure at the pump, k the Boltzmann constant, T the temperature, $2L$ the distance between pumps in a periodic vacuum structure, dI_e/dl the electron current into the wall per unit length, $d^2N_{tot}/dldt$ the particle loss per unit length and time, and

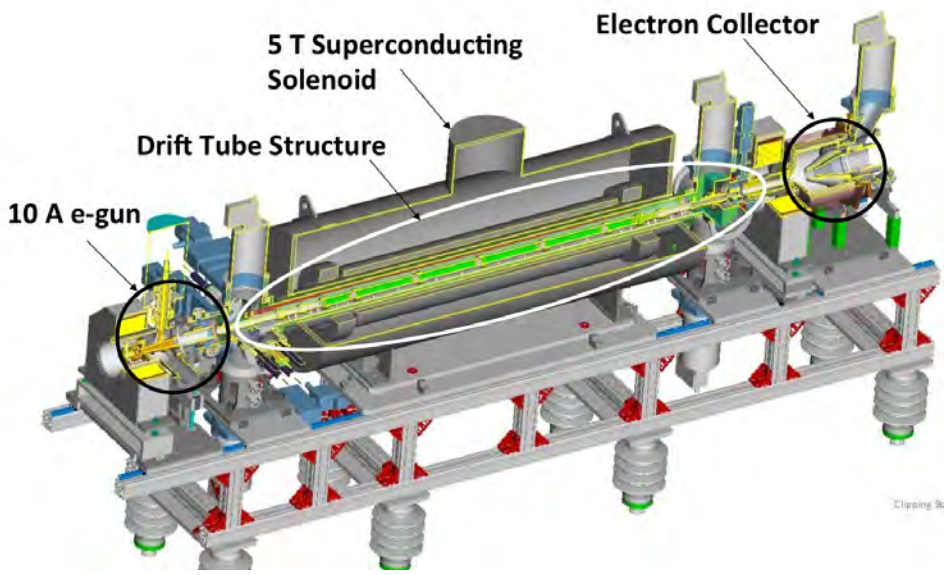

Fig. 8: Electron Beam Ion Source (EBIS) at BNL.

S the pumping speed. The parameter b is given by

$$b = \sigma_e \frac{2r}{e} \frac{dI_e}{dl} + \sigma_b \dot{N}_{\rm tot} \tag{9}$$

where σ_e and σ_b are cross sections for residual gas ionization for electrons and ion projectiles respectively. The denominator in Eq. (8) can become small, leading to pressure instabilities (see Sec. 4.1). To avoid dynamic pressure increases, Ultra High Vacuum (UHV) systems are required for most heavy-ion accelerators and storage rings. Only at the end of the ion injector chain, when the beam energy is high enough, the charge state Z is close to its maximum and the storage time short, is an unbaked vacuum system tolerable as in the Alternating Gradient Synchrotron (AGS) at BNL and the Proton Synchrotron (PS) at CERN.

3.1 Preparation of RHIC beams

3.1.1 EBIS source and Linac

Until 2012 ions were delivered by two electrostatic Tandem accelerators [46]. In 2012 a new pre-injector was commissioned, the Electron Beam Ion Source (EBIS) (Fig. 8) [47].

Beams for RHIC originate in a hollow cathode source which produces singly charged ($Z = 1$) ions through a gas discharge process in a noble gas. Two such hollow cathode sources are available, either for redundancy, two difference species, or other ion programs of the BNL hadron complex, such as the NASA Space Radiation Laboratory. In addition, a laser ion source became recently operational [48], in which the singly charged ion beam is produced by hitting a solid or frozen target with a laser beam. The laser ion source allows for rapid species switches and has the potential for increasing the intensity of ions going into the EBIS trap.

The singly charged ions from either the hollow cathode sources or the laser ion sources are then transported into EBIS. EBIS uses a 10 A electron beam in a 5 T solenoid field to both transversely constrain the ions and ionize them to a higher charge state. EBIS is followed by a Radio Frequency Quadrupole (RFQ) and a short linear accelerator (LINAC), so that all ions are accelerated to 2 MeV/nucleon. A distribution of charge states is generated in the trap, of which one is selected for injection into the Booster. The Au charge state selected is $Z = 32$ (Table 3).

3.1.2 Booster and AGS

The ions are then injected into the Booster. The Booster requires UHV in order to minimize charge change processes. In the Booster initially four bunches are merged into one in order to increase the bunch intensity. The ions are then transferred to the AGS, and all but two electrons are stripped (Table 3) [49]. These last two electrons are so tightly bound to the Au ions that the vacuum requirements in the AGS can be relaxed, and no bake-out is required. In the AGS initially eight bunches are merged into two to increase bunch intensity further. Each bunch merge at least doubles the longitudinal emittance. This is acceptable as long as the final longitudinal emittance is small enough for acceleration and storage in RHIC.

3.2 Preparation of LHC beams

3.2.1 ECR source, Linac 3, LEIR and PS

At CERN, an Electron Cyclotron Resonance (ECR) ion source is used to create the ion beam; this is followed by an RFQ and the heavy-ion LINAC3. After LINAC3 a carbon foil strips the ions to charge states around Pb^{54+}.

The ions are then accumulated, cooled, and accelerated in the Low Energy Ion Ring (LEIR) (Fig. 9) [8, 42, 50–52]. To achieve the required emittances, LEIR is equipped with an electron cooling system operating at the injection kinetic energy of 4.2 MeV/nucleon, and a transverse cooling time of 0.2 s. The nominal intensity is reached with a 71-turn injection into LEIR, and stacking in all three phase space planes. This injection process is repeated up to 6 times under continuous electron cooling. The beam is bunched on $h = 2$ and accelerated before extraction to the PS.

The LEIR vacuum system provides a dynamic pressure below 10^{-12} mbar and effects of charge exchange with the residual gas have not been significant. However recombination effects with the electron cooler beam led to a change from the original charge state of Pb^{53+} to Pb^{54+} which has a closed valence shell.

At present the intensity extracted from LEIR is substantially beyond the design value and is limited by a beam loss associated with the RF capture process after injection.

The LHC design foresaw a bunch-splitting in the PS to achieve a basic bunch spacing of 100 ns in the LHC. However various other schemes have been used in operation so far. In 2013, the bunches were injected into two adjacent $h = 16$ bunches accelerated to an intermediate 370 MeV/nucleon where a complex series of RF gymnastics were initiated using the multiple RF systems of the PS, ending with a final rebucketing to $h = 169$ in the 80 MHz system.

3.2.2 SPS and injection into LHC

The resulting bunch pair, spaced by 200 ns, was then fully stripped in the transfer line to the Super Proton Synchrotron (SPS) with a 0.8 mm thick aluminum foil in a special low-β insertion to minimize emittance blow-up. In the SPS, because of the short bunch length, intrabeam scattering and space charge at injection are the main concerns [53]. The expected space-charge tune-shift of $\Delta Q_y = 0.08$ (Eq. (6)) was found to be acceptable following successful tests with values up to $\Delta Q_y = 0.2$. Emittance growth from intrabeam scattering does not exceed 20% over the full duration of the injection plateau, and remains acceptable for injection into the LHC.

The main 200 MHz standing wave cavities of the SPS do not have sufficient tuning range to adapt to the revolution frequency of Pb beams at injection and maintain a constant harmonic number through the energy ramp, in the normal way. To overcome this difficulty a special fixed-frequency acceleration scheme [54], taking advantage of the fact that the beam fills less than a

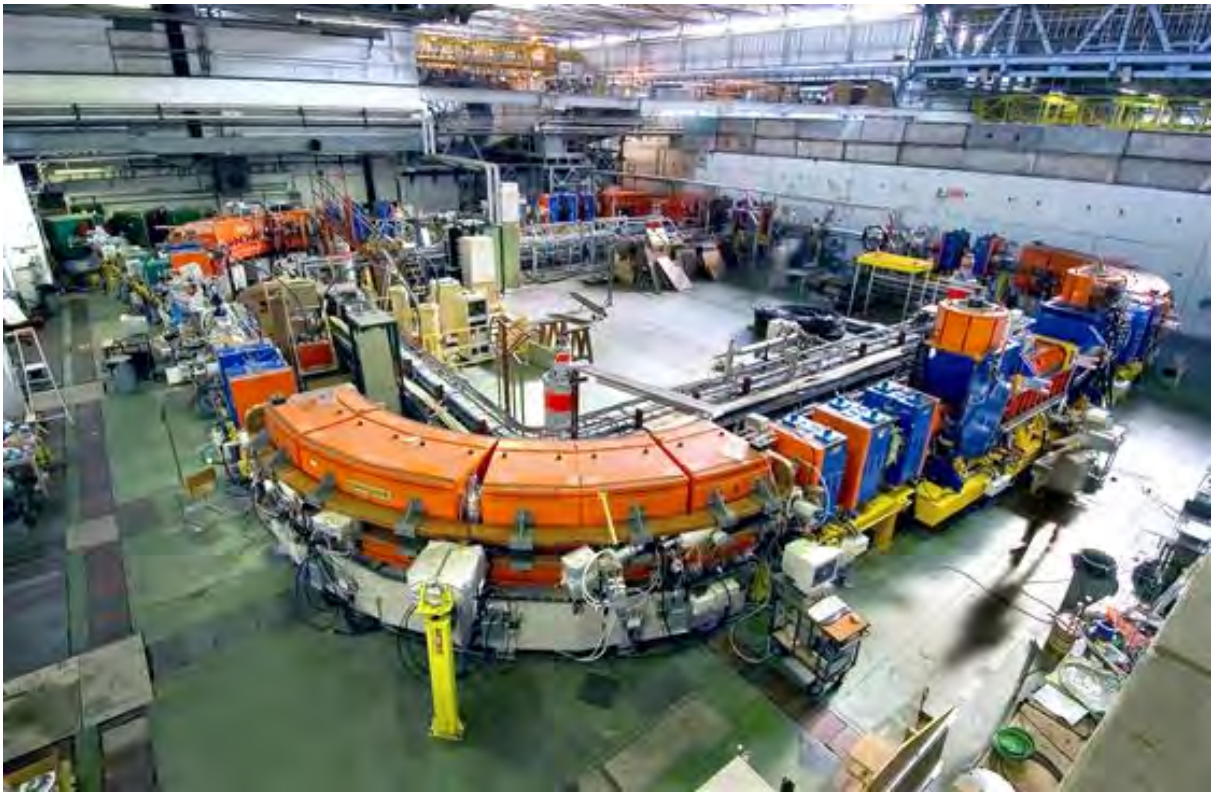

Fig. 9: Low Energy Ion Ring (LEIR) at CERN (Photo: CERN-EX-0509046).

third of the ring, has been in use since lead beams were first accelerated for the SPS fixed target program in 1994. The RF is pulsed on at the cavity center frequency during the bunch passages and switched off in the gaps while the phase is corrected before the next passage of the bunch train. In effect, the RF harmonic number is non-integer. This works successfully but enhances the RF noise seen by the beam. Combined with intrabeam scattering, longitudinal losses in the SPS are significant and most marked on the bunches which spend the longest time at the SPS injection energy. These are the earliest batches injected from the PS. An example is shown in Fig. 10.

3.2.3 Injection for hybrid collisions

For protons the LHC has a separate pre-injector system upstream of the PS. Operation as a p+Pb collider requires the two pre-injector chains to operate in parallel [55, 56]. The medium energy injectors, PS and SPS, have to alternate between accelerating the two species. Moreover, since the bunch filling pattern of the ion beam is quite different from any of those used in p+p mode, the proton injectors must operate in an unusual mode to provide a pattern identical to that of the ions. In the 2013 p+Pb run, this resulted in the SPS transferring batches of 24 bunches with an alternating 200/225 ns spacing. Deuteron-lead (d+Pb) collisions have not been requested in the LHC and would only be possible with a substantial investment in an additional source.

The LHC will most likely continue the pattern of colliding p+Pb in about one year out of three, the others being devoted to Pb+Pb. Experience with the analysis of Pb+Pb collisions of varying centrality has somewhat reduced the need perceived earlier to collide lighter nuclei. However the option to collide Ar beams, presently under preparation for the SPS fixed target program, remains under consideration. A species switch in the ion injector chain will always

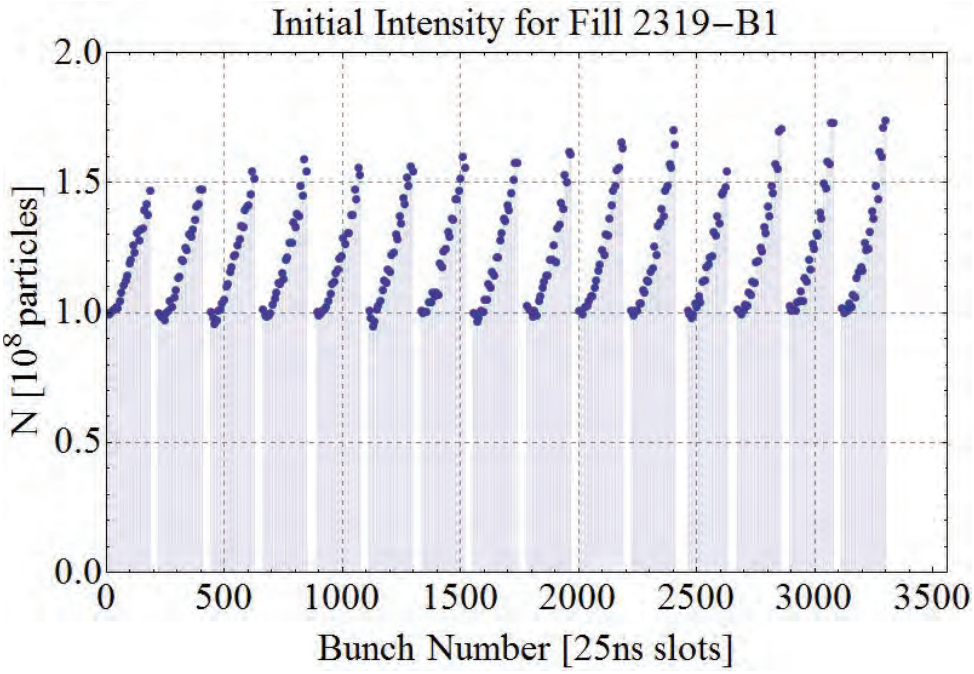

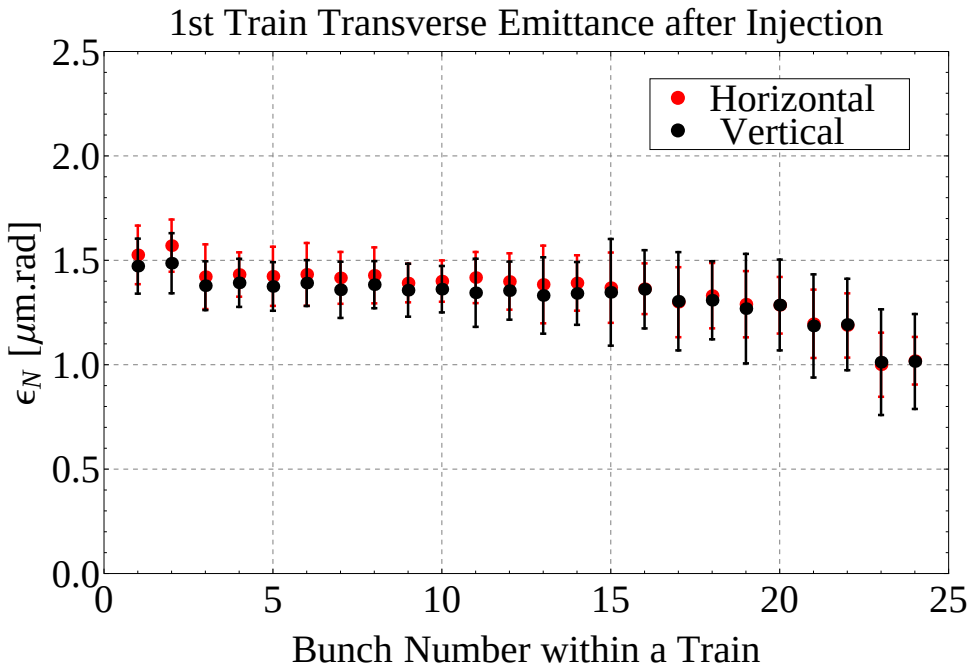

Fig. 10: Effects of IBS in SPS and LHC. Top: Variation of bunch intensity along the whole train of 358 bunches, composed of 15 SPS batches of 24 bunches each (in most cases) spaced at 200 ns, in the LHC during a Pb+Pb fill in 2011. Bottom: variation of emittance measured along a single SPS batch injected in the LHC.

take several weeks.

At the end of LHC Run 1, the Pb beam brightness delivered from the injectors exceeded the design value by a factor 3.

4 ACCELERATION IN THE COLLIDER

During beam accumulation and acceleration in the collider rings, beam loss and emittance growth is to be minimized. The ion beams are most vulnerable at injection for a number of reasons. First the beam size is at its maximum, as are the magnetic field errors of the superconducting magnets due to persistent currents. Space charge effects can lead to substantial tune spread (Eq. 6)), and intrabeam scattering (Eq. (7)) to visible beam growth. The injection of intense ion beams can be limited by dynamic pressure rises, caused by electron clouds. If uncorrected the snap-back effect at the beginning of the ramp could lead to beam loss due to rapidly changing sextupole fields. In RHIC all ions except protons have to cross the transition energy; in the LHC even the heaviest ions are injected above the transition energy. The acceleration of asymmetric species requires special attention due to the usually different charge-to-mass ratio of the two species.

4.1 Acceleration in RHIC

4.1.1 Beam accumulation

Heavy-ion beams exhibit an increase in the bunch length and transverse emittance during injection an acceleration, primarily due to intrabeam scattering effects. Accumulation of 111 bunches in one ring takes about 5 min, and bunches injected early show larger emittances in all dimensions than bunches injected late. In the early years of RHIC operation the injection of bunches with high charges of any species also created dynamic pressure increases. In Fig. 11 the measured electron flux into the wall and pressure is shown as a function of the total filled proton intensity. An analysis of the dynamic pressure rises in RHIC concluded that all operationally relevant observation are caused by electron clouds [45].

To reduce the electron cloud density a number of vacuum upgrades were undertaken, namely the baking of all warm sections, the pre-pumping of the cold beam pipes before cool-down, and the replacement of all warm beam pipes with NEG coated ones. The NEG coated beam pipes not only have a lower secondary electron yield (SEY) but also provide a large amount of distributed pumping after activation. Long operation with high intensity beam, especially protons, also reduces the electron cloud densities through scrubbing.

4.1.2 Transition crossing

RHIC is the only superconducting machine in which particles cross the transition energy. This applies to all ions except protons. A γ_t-jump is implemented with a $\Delta\gamma_t = 1$ in 30 ms in order to minimize the time near transition. Near transition the bunches are shortened, which fosters the formation of electron clouds (see pressure increase at transition in Fig. 12). This together with the increased bunch peak current and reduced synchrotron tune leads to beam instabilities.

The instabilities observed are of single bunch type and two distinct growth times have been observed (15 ms and 100 ms) [59]. Figure 13 shows a longitudinal tomographic reconstruction of a bunch that became unstable during transition crossing. Part of the longitudinal distribution is missing, showing that the transverse instability is fast compared to the synchrotron period [60].

The instabilities could be suppressed with chromaticity settings and octupoles [60], and it was found that it is advantageous to let the chromaticities cross zero shortly before transition.

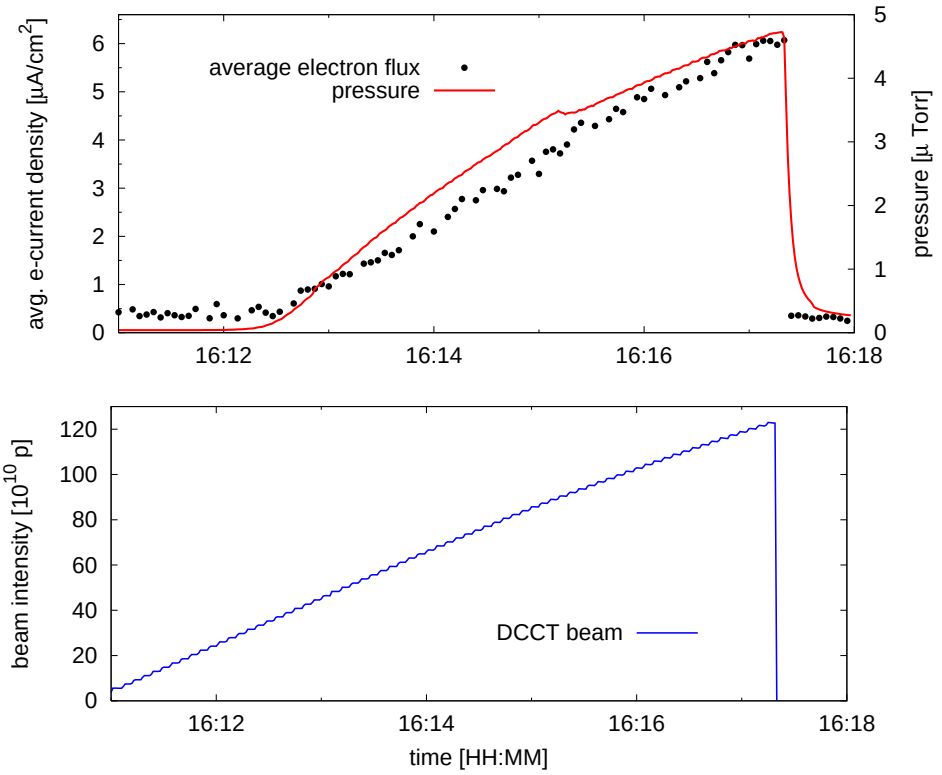

Fig. 11: Measured pressure and time-averaged electron current density into the wall (top), as beam is being injected into the RHIC Blue ring (bottom) [57].

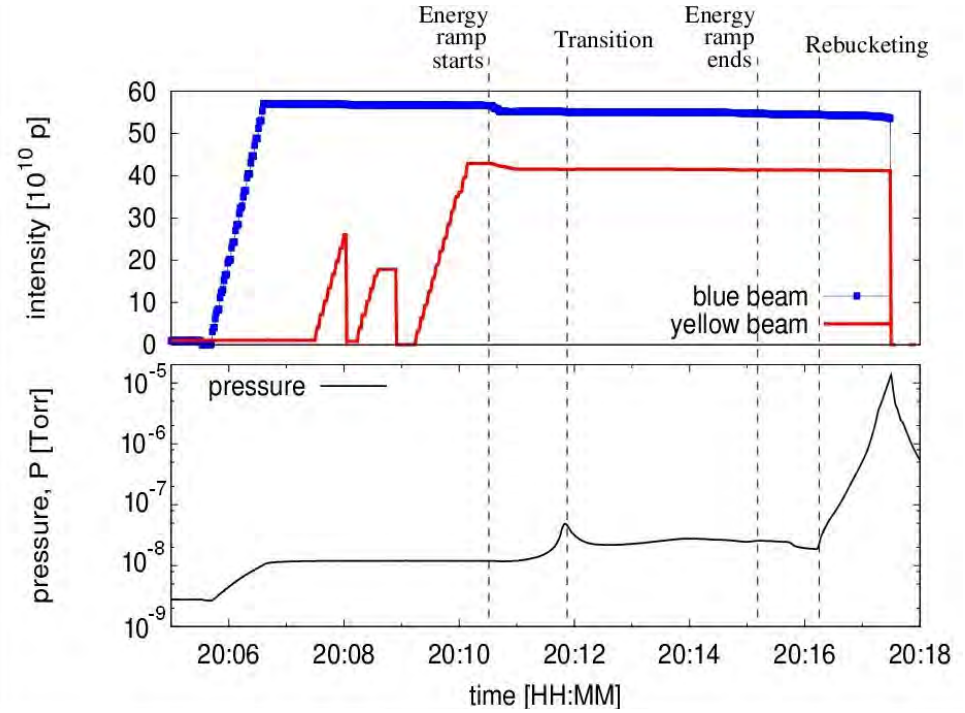

Fig. 12: A pressure instability with Au beam in the RHIC Blue ring. The upper part shows the total intensity for both rings during injection, acceleration, and storage. The lower part shows the pressure in the Blue collimator region, with an exponential increase after rebucketing [58].

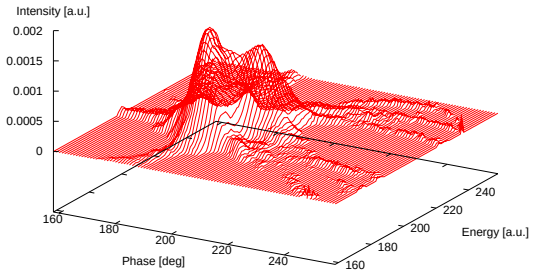

Fig. 13: Tomographic reconstruction of the longitudinal phase space distribution for a deuteron bunch that experienced a fast transverse instability at transition. (courtesy C. Montag).

The instabilities limited the bunch intensity in the past. In the most recent heavy-ion run, the intensity was not limited by transition instabilities, but by the bunch intensity available from the injectors. A long proton run in the previous year with the highest intensities so date had provided enough scrubbing to push the instability threshold beyond the available bunch intensity.

4.1.3 Rebucketing

To provide more longitudinal focusing for heavy ions at store (as a countermeasure to IBS), the bunches are transferred from an RF system with harmonic number $h = 360$ and $V_{RF} = 300$ kV, to an RF system with harmonic number $h = 7\times360$ and $V_{RF} = 3$ MV. The stronger focusing reduces the longitudinal IBS growth rates. To transfer the bunches, they are shortened by placing them temporarily on an longitudinally unstable fixed point. The shortened bunches, however, have triggered electron cloud formation, and resulted in pressure instabilities (Fig. 12). The pressure grew exponentially until the beams were aborted by the machine permit system [45]. After the vacuum upgrades in the warm sections (NEG coated beam pipes and baking), these pressure instabilities were suppressed.

4.1.4 Acceleration of asymmetric species

RHIC consists of two independent rings that only share 12 DX magnets, the dipoles closest to the interaction points that combine and separate the two beams. In this configuration the magnetic rigidities and RF frequencies of the two rings can be chosen independently as long as a beam trajectories through the DX magnets can be established.

In the first asymmetric run in 2003, d and Au beams were initially injected and accelerated with the same rigidity, resulting in different revolution frequencies [61]. This lead to modulated long-range beam-beam interactions, including tune modulations [62], which resulted in unacceptable beam loss and emittance growth. The injection and acceleration was then changed to have the same revolution frequency in both rings.

To date RHIC has accelerated d+Au, h+Au and Cu+Au beams, and plans to accelerate p↑+Al and p↑+Au (Table 1). For the latter combination the difference in the charge-to-mass ratio of the two species is large enough so that the DX magnets need to be shifted horizontally by 2 cm to establish trajectories with enough apertures.

4.2 Acceleration in the LHC

4.2.1 Switching from protons, emittance growth

The LHC has a single superconducting RF system operating at 400 MHz and capable of a peak voltage of $V_{\rm RF} = 16$ MV. Usually, $V_{\rm RF} = 8$ MV at injection and has been increased up to

Fig. 14: The first ever direct detection of synchrotron light from nuclei during the LHC ramp. The two spots are from beam 1 and beam 2 respectively.

$V_{\rm RF} = 12$ MV at collision energy. A variety of conditions have been used to optimize bunch length, losses and IBS [63].

No ion species cross the transition energy, and the magnetic settings of the injection and ramp optics have so far been kept essentially identical to those established in the preceding proton runs. With some special care to translate beam-position monitor readings from their high- to low-intensity dynamic ranges, it was possible to confirm that identical orbit and optical corrections were appropriate for particles of equal magnetic rigidity. This has been a crucial element in the extremely fast switches from proton to heavy-ion operation. Capture and acceleration of the Pb beams requires a much larger RF frequency swing between injection and collision energies.

Even at injection energy, space charge is insignificant in the LHC. Thanks to the excellent cryogenic vacuum, the beam-gas lifetime is very long (it has not been possible to measure it) and effects on emittance are negligible. Although electron cloud effects are important for protons in the LHC, the smaller charge per bunch and larger spacing of the Pb bunches reduce them to an insignificant level.

On the other hand, emittance growth and losses from the RF bucket due to IBS are significant over the half hour or so that it typically takes to fill the two rings, particularly for the batches injected earliest from the SPS. As in the SPS, this imprints a second decay pattern on the bunch intensities and emittances, batch by batch as well as within each batch (Fig. 10). Similar patterns appear in the distribution of bunch lengths although they are later largely washed out on the energy ramp.

4.2.2 Nuclear synchrotron radiation

A dramatic moment occurred in the first ramp of Pb beams in the LHC when the beam energy reached about 0.4 TeV/nucleon and an image of the beams appeared on the display of the LHC synchrotron light telescopes (Fig. 14). This was the first ever direct detection of synchrotron light from composite objects beyond electrons, positrons, protons and anti-protons, confirming that the charges of the nucleus radiate coherently [6, 64] (see also Eq. (18) later).

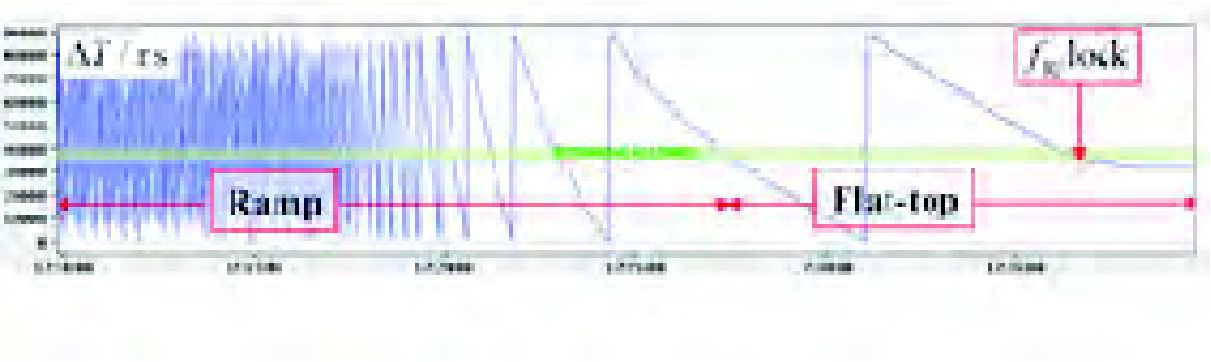

Fig. 15: Time interval, ΔT, between leading RF bucket of the p and Pb beams (scale is revolution time) during the LHC's ramp and cogging process at flat-top. The RF frequencies are locked together when ΔT is close to the value placing the encounter points of the leading buckets at the ATLAS IP, then a final adjustment is made.

4.2.3 Asymmetric acceleration for p+Pb

. Proton-nucleus collisions [55, 56] were not included in the baseline design of the LHC [6] and were first considered in 2005. With 2-in-1 magnets, both LHC rings must have the same dipole and (most) quadrupole fields. This necessitates different RF frequencies for p and Pb ions during injection and accelerations, since the radial offsets required for equal frequencies would be too large to fit into the beam pipe.

With different RF frequencies, the proton beams complete 8 more turns of the ring per minute than the Pb beams. Moving beam-beam encounters are created that lead to modulations in the long-range beam-beam interaction strength. In RHIC, a similar injection and acceleration scheme with unequal RF frequencies was abandoned (Sec. 4.1) because these effects led to emittance growth and severe beam losses during injection and ramp. The alternative of equal frequency acceleration was available to RHIC because of its separate magnetic rings but not to the LHC, leading many to doubt the feasibility of p+Pb operation. In the LHC, however, the higher beam energy and smaller bunch charge (Table 2) together with a large transverse separation and cancellations occurring among the multiple beam-beam kicks reduced the modulated beam-beam effects to an acceptable level.

The first test of injection and ramp in late 2011 validated the injection and acceleration scheme with unequal RF frequencies, and p+Pb was accepted as part of the LHC program in early 2012 [65], the first, rather unanticipated, upgrade of the machine.

At top energy, 4 TeV for protons so far, the revolution frequencies could be equalized with small orbit displacements, 0.6 mm in the arcs, of the p beam outwards, and the Pb beam inwards [56]. An efficient "cogging" process using the RF frequencies of the two rings was implemented to ensure that the correct bunches collided at each IP.

A special compensation of chromatic perturbations of each orbit during the squeeze and in collision was necessary [66].

5 LUMINOSITY LIMITATIONS

The luminosity limitations in RHIC and the LHC are somewhat different. RHIC is primarily constrained by the available bunch intensity and the effects of intrabeam scattering. While

these effects are also very important for the LHC, it is expected to be ultimately limited by secondary beams, created either in collisions (limiting peak luminosity) or collimation (limiting the value of the quotient of beam current and lifetime). The secondary beams deposit energy in cryogenically cooled magnets, which will quench if too much energy is introduced. The collision processes are also responsible for short luminosity lifetimes.

5.1 Luminosity limitations in RHIC

5.1.1 Bunch intensity.

The largest gains in luminosity can be made through an increase in the bunch intensity N_b (Sec. 2). N_b is either limited by the injectors or by instabilities near transition (Fig. 13). The achievable beam brightness N/ϵ_n is also limited by charge dependent effects in the injectors.

5.1.2 Number of bunches.

The number of bunches was limited by electron cloud induced pressure rises (see Figs. 11 and 12, and Ref. [45]). The most limiting effect was seen at store, when electron clouds were formed in some of the experiments after the bunches are transferred from the accelerating to the storage RF system. In this process the total bunch length is shortened from 10 ns to 5 ns. The induced pressure rise has produced unacceptable experimental background in the past [45]. After vacuum upgrades, the maximum number of bunches is reached, now limited by the detector electronics and injection kicker rise time.

5.1.3 Intrabeam scattering and stochastic cooling

In Fig. 16 luminosities of typical Au+Au stores are shown in 2007 and 2014. The beam lifetime 2007 is dominated by intrabeam scattering (Eq. (7)) leading to particles leaving the RF buckets. These particles are continuously cleaned out of the abort gap to avoid a quench when the beam is dumped. The luminosity lifetime is further reduced by transverse emittance growth, also predominantly caused by intrabeam scattering. To achieve a high average luminosity, stores are only a few hours long, and fast refills are required.

To overcome the beam loss and emittance growth from intrabeam scattering, three-dimensional bunched beam stochastic cooling [67] was implemented, the first operational cooling in a hadron collider. Figure 17 gives an overview of locations of the longitudinal and transverse pick-ups and kickers. With a frequency range of 5-9 GHz, cooling times of approximately 1 hour are realized.

With stochastic cooling, more than 90% of the Au ions are burned off in collisions. With U+U collisions the burn-off rate at the highest luminosities even reached 97% [68]. The high U+U burn-off rate allowed for a measurement of the total U+U cross section σ_{tot} through the measurement of luminosity and beam loss rate (for 100% burn-off $\dot{N}_b = -\sigma_{tot}\mathcal{L}_{tot}$) [68].

The comparison of the Au+Au luminosities in Fig. 16 shows a large increase in the initial luminosity from 2007 to 2014, due to an increase in the bunch intensity N_b, and an increase in the luminosity lifetime due to stochastic cooling. Over the upgrade period the average store luminosity increased by a factor of 4.2.

5.1.4 Inelastic scattering on residual gas.

Stored beam particles are lost after an inelastic collision with molecules of the residual gas in the beam pipe. The beam loss rate due to residual gas inelastic scattering of ions on molecular

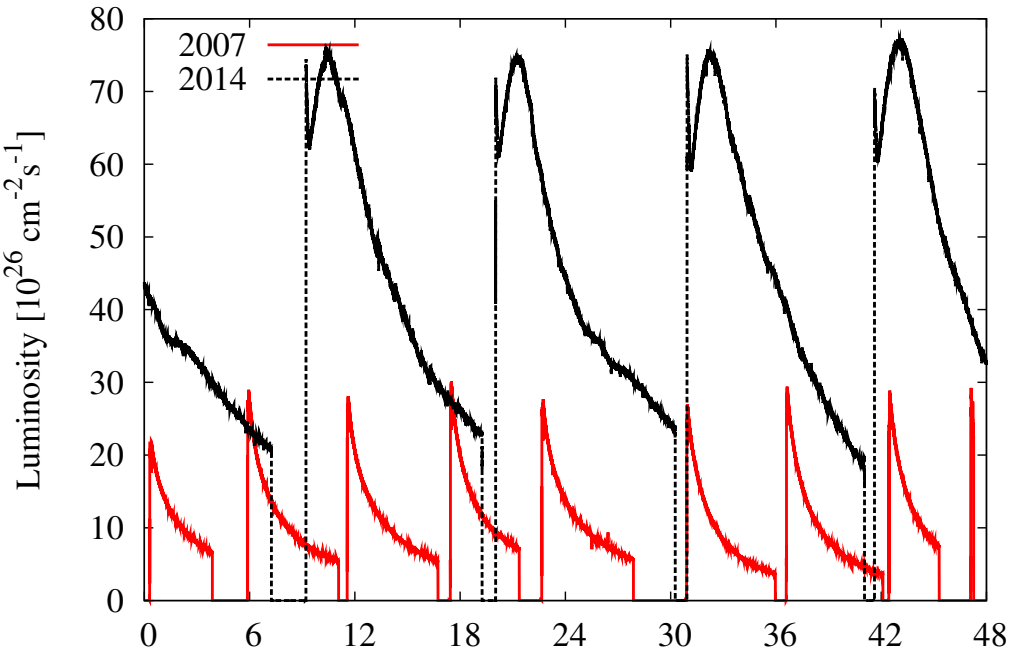

Fig. 16: RHIC luminosity delivered to the PHENIX experiment in 2007 with longitudinal stochastic cooling in Yellow Ring only, and in 2014 with three-dimensional cooling in both rings. The increase in the initial luminosity is due to an increase in the bunch intensity N_b.

nitrogen N_2 at 300 K is [69]

$$-\frac{dN_B}{dt} \approx 600\,\mathrm{s}^{-1}\mathrm{mbar}^{-1}A^{2/3}N_{B,Y}\frac{\langle\beta\rangle}{C}\int_0^C P(s)ds, \tag{10}$$

where $\langle\beta\rangle$ is the average β-function, C the machine circumference, and $P(s)$ the s-dependent N_2 pressure. The nitrogen equivalent pressure can be calculated as [69]

$$P^{nucl}_{N_2eqiv} = 0.0861\sum_i P_i \sum_j k_{ij}A_{ij}^{2/3} \tag{11}$$

where P_i is the partial pressure of gas molecules i, k_{ij} are the number of species j in the gas molecule i, and A_{ij} the mass number of species j in molecule i. Even with a UHV vacuum system the dominant beam loss mechanism for cooled heavy-ion beams in RHIC, apart from burn-off, is due to inelastic scattering on residual gas [68].

5.1.5 Beam-beam interactions.

With gold beams, the initial beam-beam parameter is $\xi = 0.0025$/IP (see Table 2) and increases to $\xi = 0.005$ with cooling. With cooling and a careful selection of the working point, beam-beam effects in symmetric heavy-ion operation are small. With asymmetric species the intrabeam scattering growth rates and cooling rates are different, which can lead to unmatched beam sizes at the interaction points. With unmatched beam sized at the IP the beam loss rate of the larger beam is enhanced. To mitigate this effect, the cooling rate of the smaller beam is reduced in order to match the beam sized at the IP [70].

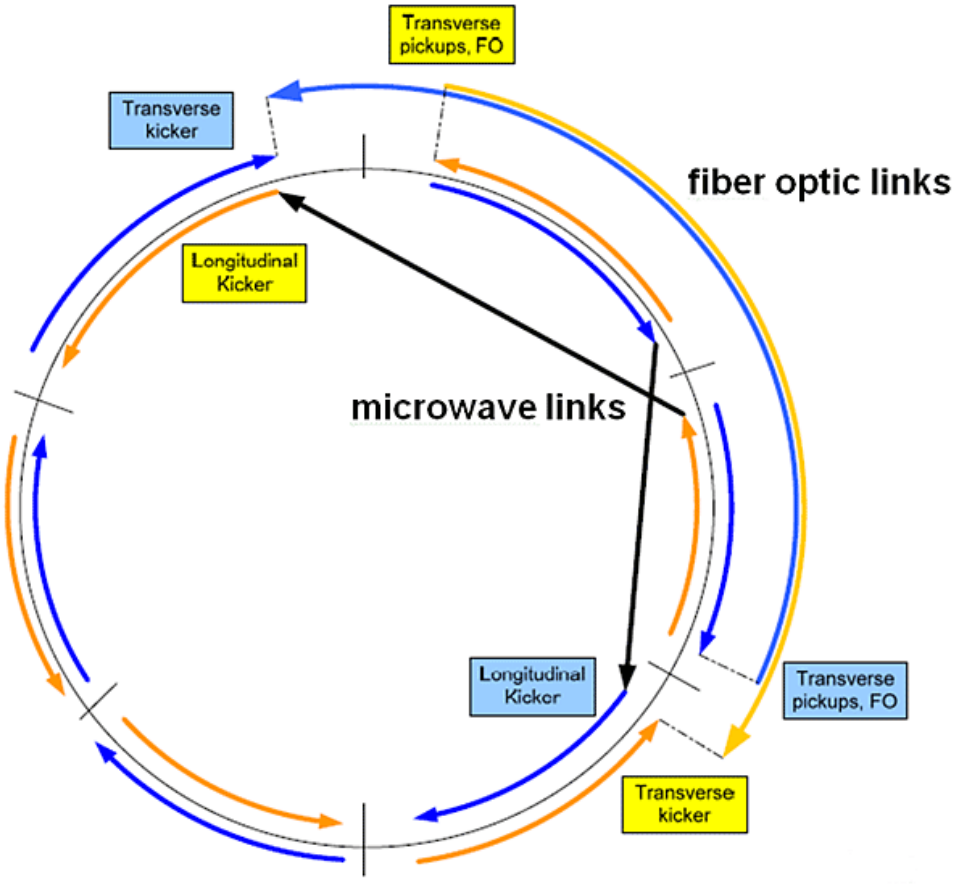

Fig. 17: Overview of the RHIC stochastic cooling system. Each plane (horizontal, vertical, longitudinal) has a pick-up and a set of kickers. Information travels from the pick-up to the kickers via fiber-optic links for the transverse planes, and via a microwave link in the longitudinal plane.

In polarized proton operation the tune spread created by head-on collisions is the dominant luminosity limitation [71]. To overcome this limit electron lenses were installed to compensate for the tune spread (Sec. 7.1).

5.2 Luminosity limitations in the LHC

Scheduling constraints are a major limitation on the integrated luminosity achievable. Annual heavy ion runs, including the time to commission the collider with new beam species, are allotted about four weeks. There is therefore a high premium on rapid commissioning using procedures especially crafted to save time.

In 2010 [63], the very first circulating Pb beams were achieved within hours and physics was declared within four days. Commissioning to an order of magnitude higher Pb+Pb luminosity was achieved in a similar time the following year. Commissioning of the completely new asymmetric p+Pb collisions was achieved within a single pilot fill in September 2012 and within a week, to gain a factor 1000 in luminosity, in the full run in early 2013 [56].

5.2.1 Optics, beam-beam separation

The optical configuration used in collisions is different from p+p in general mainly in that the β^* value at ALICE experiment has to be "squeezed" to the same small value as in ATLAS and CMS. To save time the p+p crossing angles in ATLAS and CMS are not changed. The vertical crossing angle in the ALICE experiment is generated by a combination of the permanent bump required to compensate its spectrometer magnet and an additional variable orbit bump. The Zero-Degree Calorimeter of ALICE, a detector crucial for centrality measurements, requires a small crossing angle. According to the usual criterion for separation of several rms beam sizes (σ) at parasitic beam-beam encounters [72], this is only possible with bunch spacings of a least 100 ns, the minimum Pb bunch spacing foreseen in the LHC baseline [6]. A polarity reversal of the ALICE spectrometer was requested at the mid-point of the 2011 Pb-Pb run. It was possible to save time setting this up by allowing the beams to pass through separations $< 1\sigma$ after the squeeze, proving that this separation is not a necessary condition, at least for large enough beams and low enough intensities. Beam-beam encounters at very small separation were also exploited in p-Pb operation in 2013. It may be important to exploit this in future upgrades to 50 ns bunch spacing.

The deleterious effects of the large spread in bunch parameters are compensated to a large extent by filling schemes which arrange that the parameters of individual colliding bunch pairs are mostly similar.

5.2.2 Collimation

The collimation of protons in the LHC relies on scattering on a primary collimator followed by interception on secondary collimators. For heavy ions the multi-stage principle does not work as they generally break up, by nuclear fragmentation or electromagnetic dissociation processes while interacting with the material (carbon) of the primary collimator [73–76]. This makes changes to their mass, m or charge, Q and they follow off-momentum trajectories with a fractional rigidity change

$$\delta = \frac{1 + \Delta m/m}{1 + \Delta Q/Q} - 1. \tag{12}$$

Some will be lost in the next set of bending magnets (the dispersion suppressor section of the collimation insertion). Fragments with a charge to mass ratio closer to the primary beam can travel long distances, and are like particles with large momentum errors. Secondary beams from

primary collimators (e.g. ^{206}Pb) impact cold magnets on the first pass through the interaction region 7 (IR7) dispersion suppressor. The high ionization loss also leads to a high energy deposition on the surface of the collimators.

In the LHC, only small beam losses can be tolerated to avoid quenches of the superconducting magnets, and the performance of the collimation system for heavy ions has been studied [73, 75]. Intensity limitations from collimation are expected to be comparable to those of BFPP (see below). The locations of the principal losses from these mechanisms are indicated in Fig. 20.

5.2.3 Quenches from collision products

The intense electromagnetic fields accompanying the colliding nuclei cause a number of ultra-peripheral (meaning that the nuclear radii do not overlap) interactions which make changes to their mass and charge [77–82].

In the case of the Pb+Pb collisions in the LHC, these include, with the highest cross-section, the first-order bound-free pair production (BFPP1):

$$^{208}\mathrm{Pb}^{82+} + ^{208}\mathrm{Pb}^{82+} \rightarrow ^{208}\mathrm{Pb}^{82+} + ^{208}\mathrm{Pb}^{81+} + \mathrm{e}^{+} \tag{13}$$

with $\sigma = 281\,\mathrm{b}$, $\delta = 0.01235$. The double bound-free pair production process (BFPP2):

$$^{208}\mathrm{Pb}^{82+} + ^{208}\mathrm{Pb}^{82+} \rightarrow ^{208}\mathrm{Pb}^{82+} + ^{208}\mathrm{Pb}^{80+} + 2\mathrm{e}^{+} \tag{14}$$

has a much lower cross-section. More significant processes are electromagnetic dissociation with emission of a single neutron (EMD1):

$$^{208}\mathrm{Pb}^{82+} + ^{208}\mathrm{Pb}^{82+} \rightarrow ^{208}\mathrm{Pb}^{82+} + ^{207}\mathrm{Pb}^{82+} + \mathrm{n} \tag{15}$$

with $\sigma = 96\,\mathrm{b}, \delta = -0.00485$, or two neutrons (EMD2):

$$^{208}\mathrm{Pb}^{82+} + ^{208}\mathrm{Pb}^{82+} \rightarrow ^{208}\mathrm{Pb}^{82+} + ^{206}\mathrm{Pb}^{82+} + 2\mathrm{n} \tag{16}$$

with $\sigma = 29\,\mathrm{b}, \delta = -0.00970$. The cross-sections for these processes are much larger than those of the hadronic interactions, $\sigma = 8$ b, that occur when the nuclei overlap and which are the main object of study of the experiments.

For the LHC, the consequences of BFPP1 in particular have been discussed in Refs. [79, 80] and in most detail in Ref. [82]: the secondary beams hit the beam pipe in the dispersion suppressor, depositing enough power to potentially quench a superconducting dipole magnet, as illustrated for ALICE in Fig. 18. Note that the secondary beams are smaller than the main beam because their source is the luminous region, not the beam distribution.

The losses corresponding to these effects were clearly detected in the 2010 and 2011 Pb+Pb operation and are the most prominent peaks visible in Fig. 20. Figure 19 is a more detailed view of the region shown in Fig. 18, with beam-loss monitor signals peaking at the predicted location of the BFPP1 loss.

Estimates of the energy deposition likely to quench the superconducting cable of the LHC magnets have become steadily higher [82, 83] and it now seems likely that the LHC will be able to exceed the design luminosity. In Run 2, when the magnets will be operating much closer to their full field and are more susceptible to quenches, a mitigation strategy involving the spreading out of the losses with orbit bumps will be implemented. This was tested successfully in 2011.

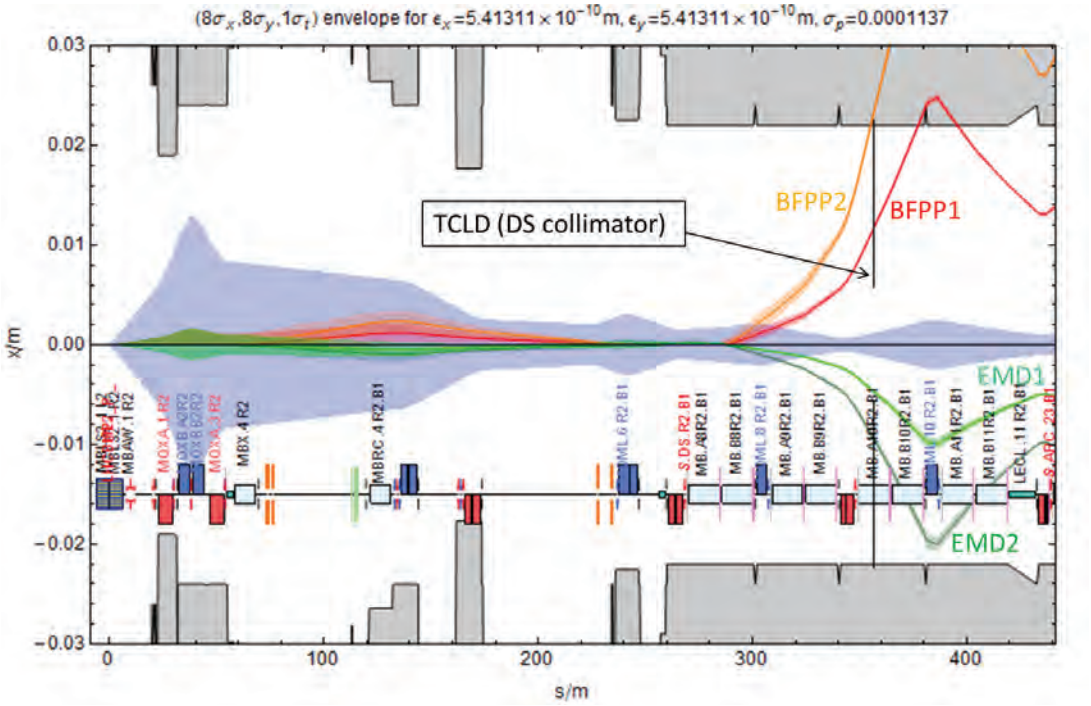

Fig. 18: Calculated trajectories of secondary beams from Pb+Pb collisions in the LHC from beam 1 in IR2. The 8σ circulating Pb beam envelope is shown in light blue. Secondary beams from BFPP1 and BFPP2 are lost in the dispersion suppressor. Only 1σ envelopes of the secondary beams are shown; they are a further factor $\approx 1/\sqrt{2}$ smaller than the main beam since their source is the luminous region around the IP. The "TCLD" is explained in Sec. 7.2.

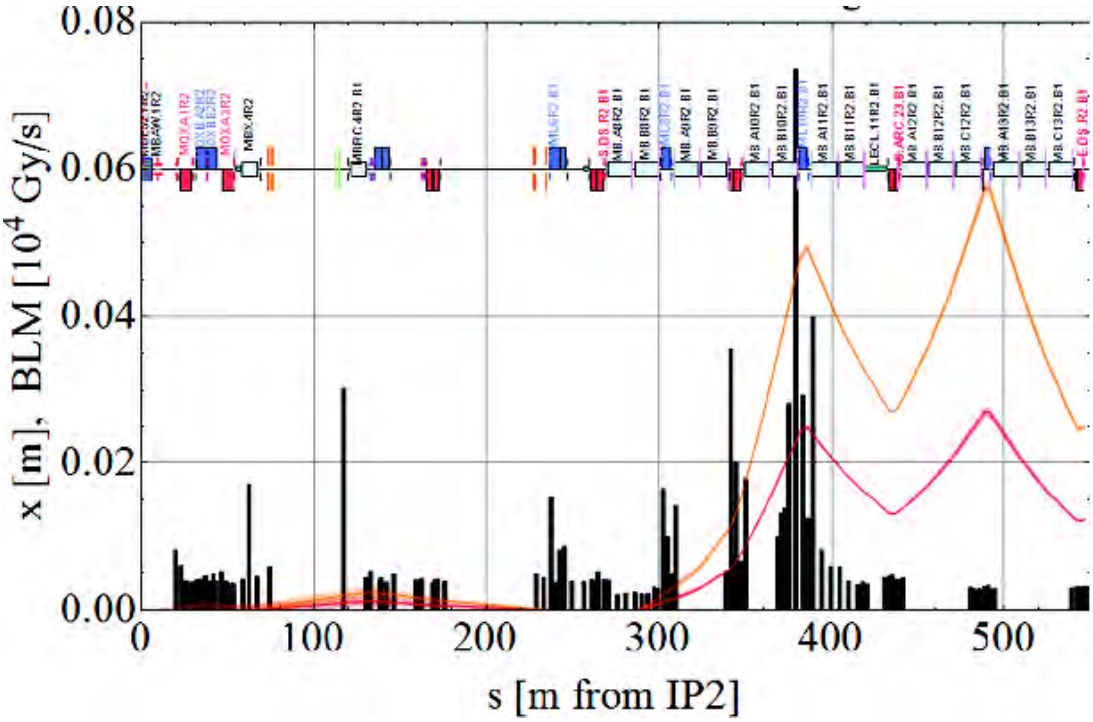

Fig. 19: Close-up of the main loss location of the the BFPP1 beam with beam-loss monitor signals from LHC operation superposed.

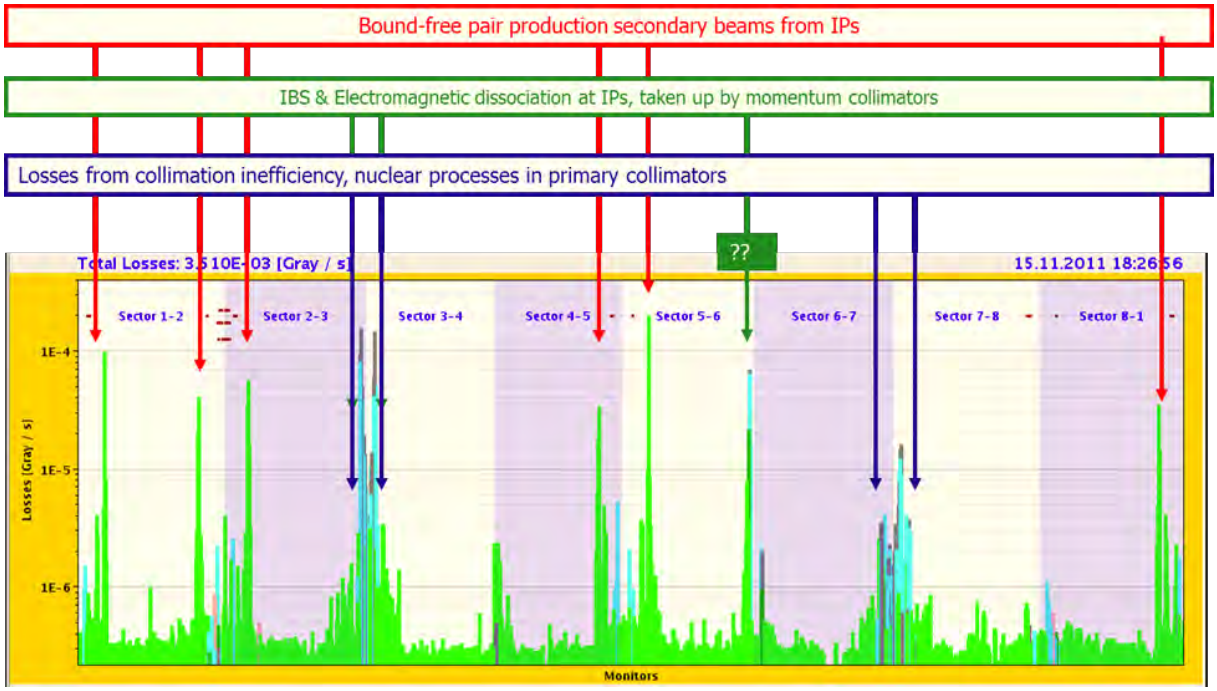

Fig. 20: Measured beam losses and identification of corresponding nuclear processes around the LHC ring during Pb+Pb collisions in 2011.

For comparison, in RHIC Au^{78+} beams created by BFPP1 are within the momentum aperture, and are therefore not all lost in a single location. The loss of a secondary Cu^{28+} beam with a higher value of δ (Eq. 12), created by BFPP1, could be observed for the first time 141 m from the interaction point of a high-luminosity experiment with especially installed PIN diodes [84]. Because of the much smaller cross section in this case, the deposited energy did not create any operational problem.

Figure 20 shows the combined effect of the various loss mechanisms as seen by the beam-loss monitors that are densely disposed around the LHC ring together with an identification of the principal peaks based on present understanding. Some of the smaller loss peaks remain to be identified. These monitors are an essential part of the machine protection system and can trigger a dump of the beams when losses exceed pre-determined thresholds. During heavy-ion operation these thresholds have been cautiously and progressively raised, sometimes by absolute necessity, but so far no beam-induced magnet quenches have occurred. From 2015 onwards, the magnets will be operating at much higher field and the tolerable steady-state energy deposition values will be lower. Moreover the power deposited, at least by the luminosity losses, will increase in proportion to $E\mathcal{L}$ further worsening the situation.

These collision processes occur in every illuminated experiment and dominate the "burn off" [69] of particles from the beam

$$\frac{dN}{dt} = -\sigma_{\text{tot}} \Sigma_{\text{experiments}} \mathcal{L} \tag{17}$$

where σ_{tot} is the total cross-section and already dominate the decay of luminosity at the LHC [35, 81, 85]. At higher energy and luminosity, the luminosity decay will be even faster.

5.2.4 *Radiation damping*

In terms of the proton mass, the mass of the $^{208}\mathrm{Pb}^{82+}$ nucleus is $m_{\mathrm{Pb}}/m_{\mathrm{p}} = 206.43$ and its energy is $E_{\mathrm{Pb}} = ZE_p = 574\,\mathrm{TeV}$ at the design magnetic field of the LHC. Since the wavelengths of the synchrotron radiation emitted by the Pb ions are in the ultraviolet range, far larger than the nuclear radii themselves, one can expect the $Z = 82$ charges of the nucleus to radiate coherently like a single charge. The synchrotron radiation damping rate for the *horizontal emittance* of a particle of mass m, charge q and energy E in a ring with bending radius ρ and revolution frequency f_0, is

$$\frac{1}{\tau_\varepsilon} = \frac{4\pi}{3c^8}\left(\frac{q^2}{4\pi\varepsilon_0}\right)\frac{f_0}{\rho}\frac{E^3}{m^4}. \tag{18}$$

Comparing a Pb ion, with $q = Ze$, to a proton in the same ring, one finds that

$$\frac{\tau_{\varepsilon\mathrm{p}}}{\tau_{\varepsilon\mathrm{Pb}}} = \frac{Z^5}{\left(m_{\mathrm{Pb}}/m_{\mathrm{p}}\right)^4} \approx 2.04,$$

that is, the radiation damping for heavy ions is *twice as fast* as for protons *in the same magnetic ring*. At the LHC design energy $\tau_{\varepsilon\mathrm{Pb}} \approx 12.7\,\mathrm{h}$, which is comparable to the IBS growth times for the design bunch intensity and will have a beneficial impact on luminosity performance and beam losses, particularly as the bunch intensity decays.

Figure 21 shows the luminosity decay in a Pb-Pb fill compared with a model that reconstructs it as the sum of individual bunch pair luminosities [35]. The model includes the physics of IBS, luminosity burn-off, radiation damping and other effects.

5.2.5 *Asymmetric p+Pb performance*

The first short p+Pb run of only 16 h took place in 2012 and proved to be extremely valuable both as the first trial of this new operational mode of the collider and the preparation of the experiments' triggers but also in terms of unexpected physics results (see Section 1). Collision condition set-up and data-taking were achieved in a single fill using the ramp optics and procedures carefully designed to respect the machine protection constraints. Also moved IP for ALICE. For the main p+Pb run in early 2013, both injector chains were recommissioned, for the special p+Pb filling pattern, within one month and the luminosity goal of 30 nb^{-1} was reached, equivalent to the nucleon-pair luminosity of the previous Pb+Pb runs (as seen in Fig. 6). In addition, p+p reference data were provided at the same energy per nucleon.

The optics provided low $\beta^* = 0.8\ m$ values not only at the usual heavy-ion experiments ATLAS, ALICE and CMS but also $\beta^* = 2.0\ m$ at LHCb. This required a modification to the filling pattern in which bunches from two SPS batches in one beam were displaced in time to collide at LHCb.

The beam sizes at the IP were different, with proton bunches smaller than the Pb bunches. Because of the variations in the emittances in the p and Pb bunches there were numerous classes of bunch-bunch combinations with a wide spread in lifetimes and very close parasitic encounters around ALICE for the bunches designed to collide in LHCb.

The main performance limitation came from the beam positions monitors (BPMs), which triggered dumps when the intensity of some bunch became too low.

Examination of the 2013 luminosity accumulation in Fig. 6 illustrates the variety of physics conditions that were requested by the experiments: In the middle of the run, the beams were reversed (p+Pb became Pb+p) and the two rings had to be set up again with interchanged RF ramps and reversed chromatic shifts in collision. In order to collect minimum-bias data, ALICE

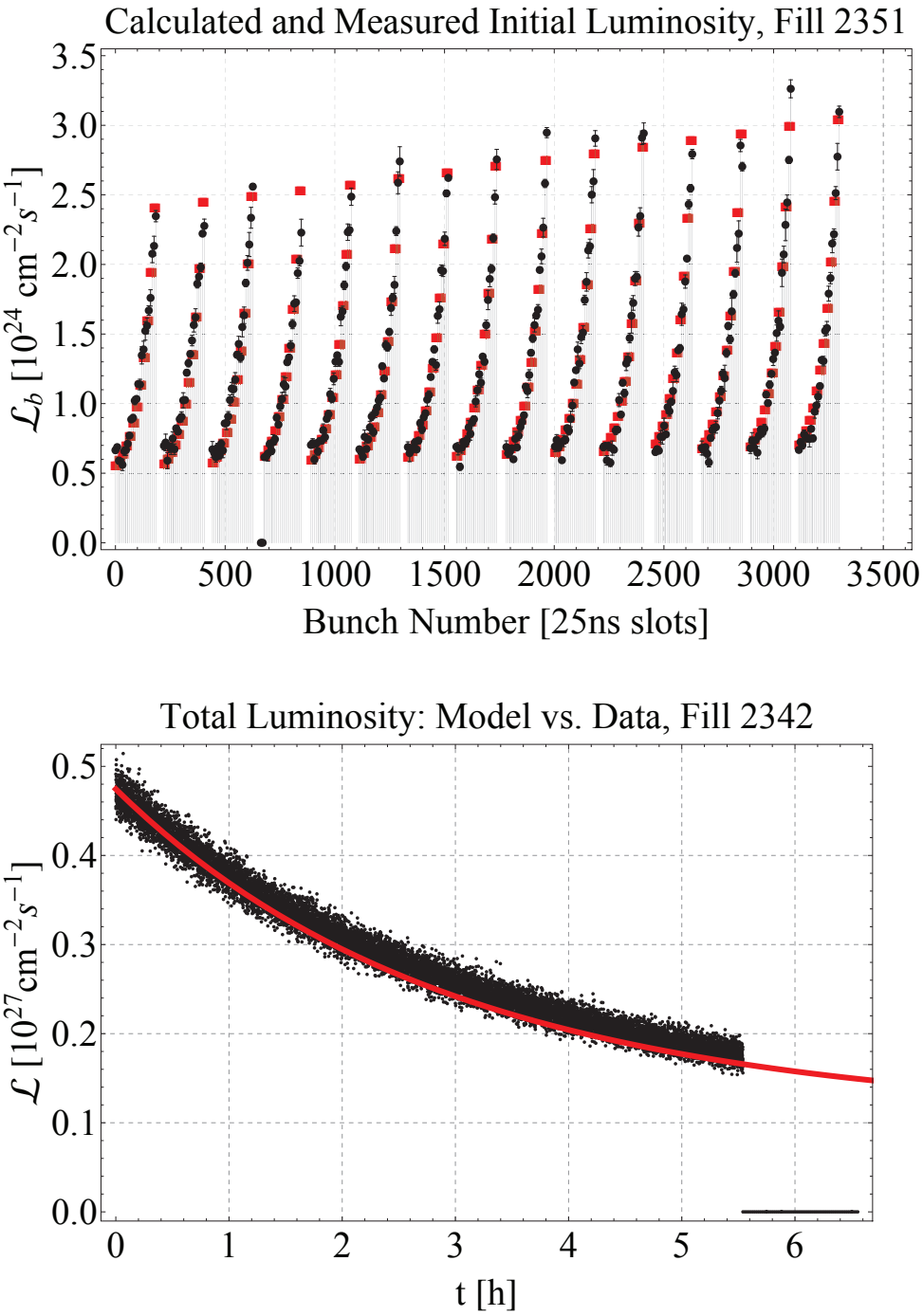

Fig. 21: Top: calculated and measured bunch-pair luminosity in the LHC at the start of a fill during the 2011 Pb+Pb run. Bottom: total luminosity summed over all bunch pairs and reconstructed from simulations of individual bunch pair evolutions [35].

requested low luminosity in the first few days, simultaneously with maximum luminosity at ATLAS and CMS. This was achieved by a luminosity-leveling procedure, in which the beams were partially separated in the horizontal non-crossing plane. ALICE's luminosity deficit was compensated later by catch-up fills where ATLAS and CMS did not receive collisions so that the luminosity lifetime became much longer. In this way, all three experiments ended the run with very similar integrated luminosity. A reversal of detector solenoids and, therefore, crossing angles, was also requested by ALICE and LHCb.

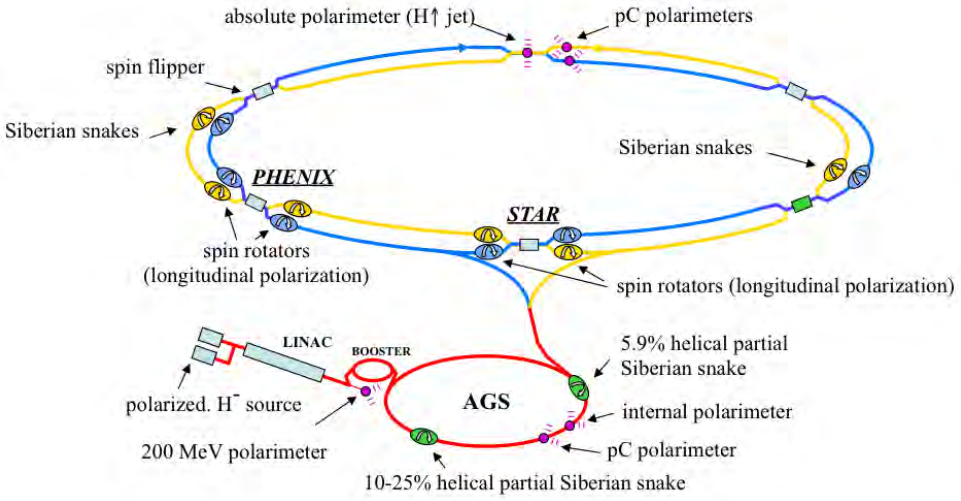

Fig. 22: Special elements for polarized proton operation in RHIC.

6 POLARIZED PROTONS AT RHIC

RHIC holds the record for the highest energy polarized protons (Table 4) [86] and is the world's first and only collider of polarized protons [87]. In polarized proton operation both luminosity $\mathcal{L}$ (Eq. (3)) and polarization P are of great importance since the experimental figure of merit is $\mathcal{L}P^2$ for single-spin experiments and $\mathcal{L}P^4$ for double-spin experiments [88].

Unlike electrons and positrons, protons do not self-polarize due to the absence of synchrotron radiation. They need be created in a polarized source, and the polarization must be maintained to a large degree throughout the accelerator chain. A number of specialized elements are needed for polarized proton operation (Fig. 22): a polarized source, snakes and rotators (devices that change the spin direction), and polarimeters (devices that measures the polarization). Table 4 shows the main parameters for the polarized proton operation, and Fig. 23 the evolution of the integrated luminosity and average store polarization over the operating years.

In the source [89] the valence electron of an alkali metal (Rb) is polarized through optical pumping, and then attached to proton. The electron spin is transferred to the proton in a so-called Sona transition [90], a section in which the longitudinal field is reversed. The then neutral hydrogen atom picks up another electron in a sodium curtain to form H^- for acceleration in the 200 MeV Linac.

The polarized source was upgraded several times leading to both higher intensity and polarization. The latest upgrade is expected to increase the source intensity by up to an order of magnitude [89]. The high intensity will be used to retain the well-polarized core of the beam, and still allow for higher bunch intensities N_b in RHIC to increase the luminosity.

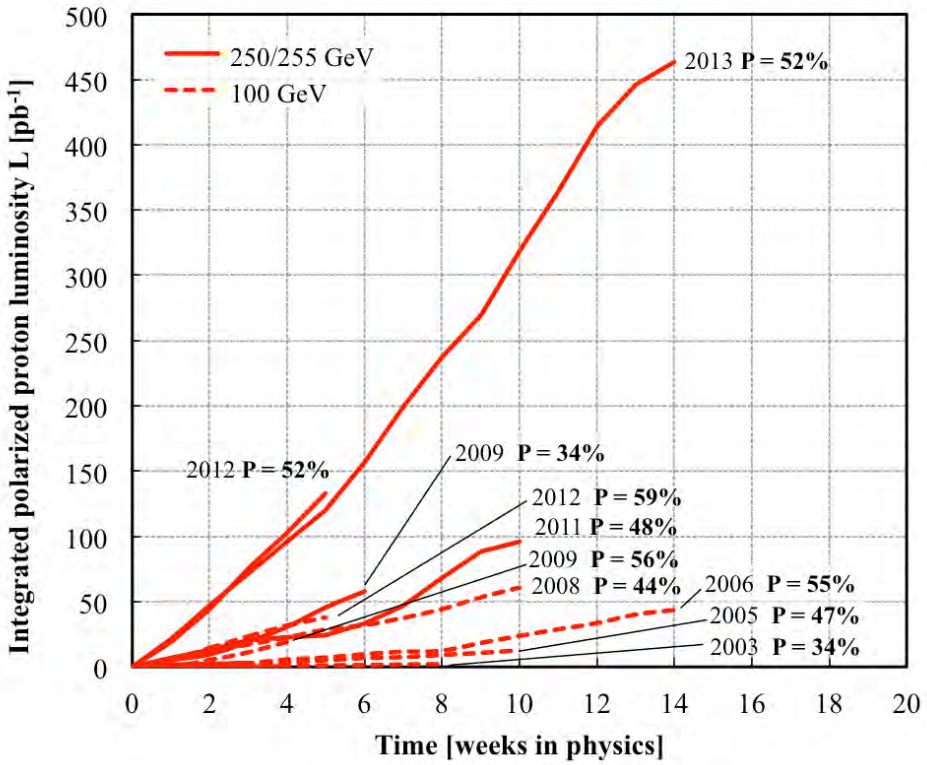

Fig. 23: Integrated polarized proton luminosity L and average beam polarization delivered to PHENIX, one of the two high-luminosity experiments at RHIC [5].

Table 4: Main parameters for polarized proton beams in RHIC. Unless noted otherwise parameters are given for the beginning of store.

parameter	unit	design 2004	achieved 2012	upgraded $\geq$2016
beam energy E	GeV	100 / 250	100 / 255	100 / 255
bunch intensity N_b	10^{11}	2.0 / 2.0	1.6 / 1.85	2.5 / 2.5
no of bunches k_b	...	111	111	111
normalized rms emittance ϵ_n	μm	2.5	3.3 / 3.1	3.0
rms bunch length σ_s	m	0.87 / 0.55	0.63 / 0.60	0.60 / 0.55
beam-beam parameter ξ/IP	10^{-3}	9.6	5.9 / 7.2	10 / 10
stored beam energy	MJ	0.36 / 0.87	0.27 / 0.84	0.45 / 1.13
peak luminosity L_{peak}	10^{30} cm^{-2}s^{-1}	90 / 250	46 / 245	150 / 500
average luminosity L_{avg}	10^{30} cm^{-2}s^{-1}	60 / 150	33 / 160	90 / 300
average polarization P	%	70	59 / 52	70

In flat rings with only vertical magnetic fields the vertical spin direction is stable as the spin precesses around the vertical magnetic fields that bend the proton trajectories. The number of precessions per turn is the spin tune $Q_{sp} = G\gamma$, where $G = 1.7928$ is the anomalous gyromagnetic ratio of the proton. However, to ensure the stability of orbital motion, horizontal magnetic fields are needed in quadrupoles. The horizontal fields can resonate with the spin precession due to the finite beam size, which give rise to intrinsic resonances ($G\gamma = kM \pm Q_y$ where k is an integer, M is the super-symmetry of the ring and Q_y the vertical tune). The horizontal fields also resonate with the spin tune $G\gamma$ due to vertical orbit errors through imperfection resonances ($G\gamma = k$) [91]. With snakes the harmful effects of depolarizing resonances can be overcome. In the AGS there are a warm and cold snake (Fig. 22). The AGS also has two fast quadrupoles installed to jump over 80 relatively weak horizontal depolarizing resonances [92].

The RHIC snakes are installed in opposite locations in both rings, and flip the spin from up to down, or down to up thereby canceling depolarizing effects that build up over many revolutions. Spin rotators near the experiments rotate the spin from the stable vertical direction in the arc into the longitudinal direction in the experiments, and back.

An important aspect of the polarized proton program is polarimetry. An absolute measurement of the polarization in RHIC is provided by a polarized atomic hydrogen jet [93]. These measurements take several hours. A fast measurement is provided with an ultra-thin carbon target [94], which needs to be calibrated with the hydrogen jet. Since polarization measurements are slow and have a relatively large error is it not possible to tune the machine based on polarization measurements. Rather machine setup and tuning must rely on measured beam properties such as orbit deviations, tunes, coupling, and chromaticity.

The orbit, tune and coupling feedback [95] was particularly useful for the polarized proton operation, since it allowed control of the orbit deviations within a few percent of the beam size. It also allowed to accelerate the beam close to a low-order orbit resonance, where the polarization transmission is highest.

7 UPGRADES

Upgrades for RHIC and the LHC aim for greater physics potential through an increase in the luminosity, new species combinations and extensions of the energy range. In the case of RHIC it also includes increases in the proton polarization, and the addition of polarized ^{3}He beams. Both RHIC and LHC can also be the basis for an electron-ion collider, eRHIC [96,97] and LHeC [98] respectively, through the addition of an electron accelerator. In both cases the preferred upgrade option for the electron accelerator is now an energy-recovery linac (ERL), which allows for larger hadron beam intensity since a larger beam-beam parameter (disruption parameter) can be tolerated in the electron beam. Electron-ion colliders are covered in more detail elsewhere [99].

7.1 RHIC upgrades

Upgrades in RHIC are in three areas, namely for high energy ion operation, for low-energy ion operation, and for polarized beam operation.

7.1.1 High energy ions.

With the full implementation of 3D stochastic cooling a major upgrade phase came to an end in 2014 (Fig. 16), resulting in an average store luminosity larger than the design value by a factor of 25 and operational stability at an unprecedented level. A further increase in the heavy ion-luminosity by a factor of two is possible from two sources: (i) an increase in the bunch intensity due to the laser ion source, and (ii) the full commissioning of the 56 MHz SRF cavity.

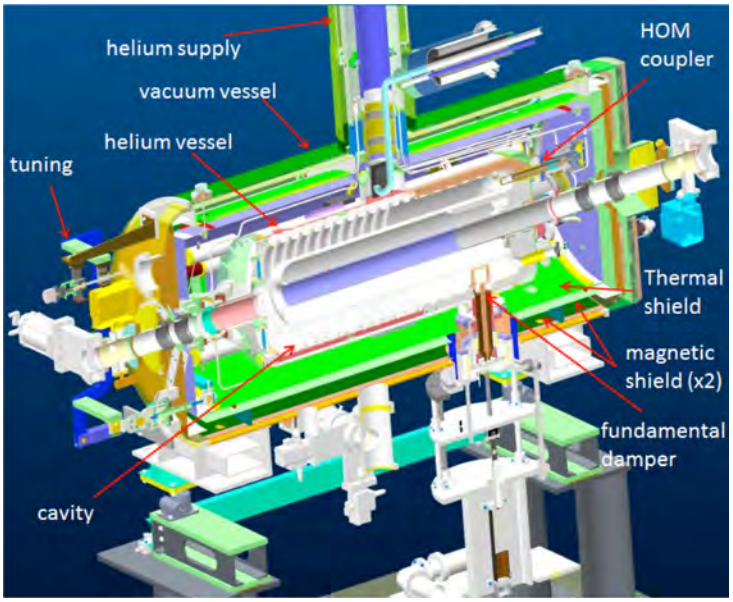

Fig. 24: Superconducting 56 MHz RF cavity in RHIC.

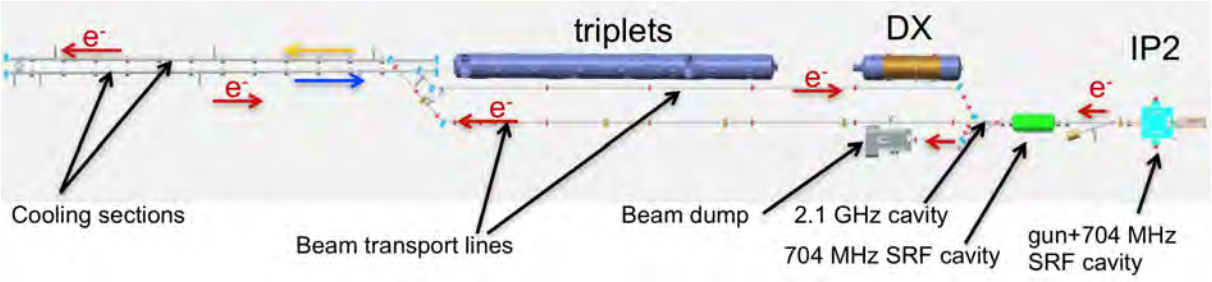

Fig. 25: Layout of the Low-Energy RHIC electron Cooler (LEReC).

An increase in the bunch intensity of 20% is possible with the new laser ion source [48]. The source can already match the performance of a hollow cathode source, and exceed it with an upgrade. In the past the intensity was limited by a fast transverse instability at transition. In 2014 no instability was observed, neither beam loss nor emittance growth. Likely, the long polarized proton run with high intensity beam in the previous year scrubbed the arc beam pipes sufficiently to suppress electron clouds in the arcs. Furthermore, a new 9 MHz RF system is under construction, which can be used to lengthen the bunches at transition in order to reduced the beam peak current and electron cloud density. Simulations show that the 3D stochastic cooling systems can accommodate bunch intensities up to 2×10^9 Au ions (Table 2). The higher bunch intensity also requires an upgrade of the exit window of the beam dump system to allow for the increased energy density.

A new 56 MHz SRF system (Fig. 24) ran in 2014 with 300 kV gap voltage, limited by quenches in the Higher Order Mode (HOM) damper. The cavity is a quarter-wave resonator in which the voltage is generated by the hadron beam. With a modification of the HOM dampers the design voltage of 2 MV can be reached, and with the increased longitudinal focusing an increase in the average store luminosity of 30-50% is expected [100].

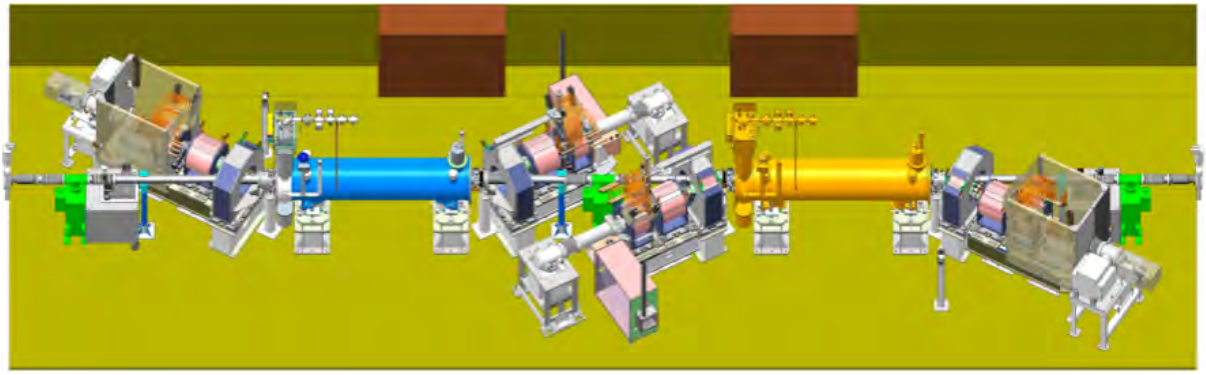

Fig. 26: Layout of the 2 RHIC electron lenses in an interaction region.

7.1.2 Low energy ions.

In search of the critical point in the nuclear phase diagram at energies below the nominal injection energy, an order of magnitude increase in luminosity is needed. At the low energies space charge and intrabeam scattering is particularly strong, and only with cooling are large increases in the luminosity possible.

A number of cooling techniques are available at this energy. For example, a DC electron beam as was used in the cooling of anti-protons in the Fermilab recycler [101]. The cooling approach selected for the low-energy program of RHIC is non-magnetized bunched beam electron cooling [102]. Figure 25 shows the layout of the cooling section with a gun and 704 MHz 1/2 cell SRF cavity, a 704 MHz 5-cell SRF acceleration cavity, a 2.1 GHz warm cavity for energy spread correction, beam transport lines and cooling sections. The electron beam cools first the Yellow beam, is turned around, and then cools the Blue beam.

7.1.3 Polarized beams.

For polarized protons an increase in the average luminosity by a factor of two is targeted at both 100 GeV and 255 GeV beam energy. The primary luminosity limitation in polarized proton operation is the head-on beam-beam effect, which leads to unacceptably large tune spread and the enhancement of resonance driving terms (RDTs).

The tune spread can be reduced again if the proton beam collides with a low-energy electron beam (electron lens [103]), in addition to the two head-on collisions with the other proton beam. The low-energy electron beam must provide the same amplitude dependent force, but with the opposite sign, as the proton beam. To stabilize the low energy beam, the electron-proton interactions take place inside a solenoid with up to 6 T field. Two electron lenses were installed and are under commissioning [104, 105]. Figure 26 shows the layout of the RHIC electron lenses in one of the six interaction regions. The two superconducting solenoids have the opposite polarity to minimize their combined effect on coupling and spin. For beam-beam compensation to be effective, the betatron phase advance between the proton-proton and proton-electron interaction must be a multiple of π so that beam-beam RDTs are minimized.

In addition to polarized protons, experimenters would like to have polarized neutrons. The easiest way to provide these in RHIC is in the form of polarized ^{3}He. A source was developed at MIT [106, 107], and unpolarized ^{3}He was already used in RHIC operation in h+Au collisions (Table 1). An upgrade to the polarimeters is also necessary, and 6 instead of only 2 snakes may be required to preserve the polarization of ^{3}He in RHIC (with $G = -4.19$ twice as many imperfection resonances have to be crossed than for protons) [108]. Polarized ^{3}He is also an important species for the electron-ion collider eRHIC.

7.2 LHC upgrades

The LHC upgrades address the heavy-ion luminosity limitations stemming from the intensity and number of bunches, the unavoidable loss of secondary beams in the dispersion suppressors and the rapid loss of beam intensity from luminosity burn-off. They are seen as an integral part of the High-Luminosity LHC project [109] in the early 2020s. However the major elements for upgrading the heavy-ion luminosity should be in place a few years earlier. At that point the ALICE experiment is expected to have been upgraded to accept peak luminosities of up to $7 \times 10^{27}\,\mathrm{cm}^{-2}\mathrm{s}^{-1}$.

7.2.1 Ion injectors.

Changes in the injector chain include work to increase the output from LINAC3, and reduce losses from high-intensity beams in LEIR. This will allow a new bunch-splitting scheme in the PS to avoid exceeding the space-charge and IBS limits at the injection energy. With an upgraded SPS injection kicker and, possibly, a slip-stacking injection scheme, shorter bunch spacing and up to twice as many bunches k_b/ring will be possible (Table 2), with a target bunch intensity of up to 0.12×10^9.

Other schemes without splitting in the PS and fewer bunches might allow a bunch intensity of 0.22×10^9, a three-fold increase over the design value (Table 2) at the price of shorter luminosity lifetime. In all cases the key to higher integrated luminosity in the strong burn-off regime will be to inject as many ions as possible into the LHC, with less emphasis on peak luminosity.

7.2.2 Collimation.

The losses of secondary beams created by BFPP lost in the cold dispersion suppressor are estimated to limit the Pb+Pb peak luminosity to $\simeq 3\times10^{27}\mathrm{cm}^{-2}\mathrm{s}^{-1}$. This limit can be overcome by installing special collimators (indicated as TCLD in Fig. 18) in the dispersion suppressors of the collimation insertions (Fig. 27) which could selectively absorb the secondary beams.

A dispersion suppressor collimator consists of two 5.5 m long 11 T dipoles [110], and a 3 m long cryogenic bypass that can accommodate a 1 m long warm collimator [111]. Such a unit can replace a standard LHC dipole with a nominal field of 8.33 T and provide the same bending strength [111]. With the collimators in the dispersion suppressor of either side of a given experiment, the peak luminosity can be doubled, and is then constrained by the injector performance.

7.2.3 Stochastic cooling.

The implementation of stochastic cooling for heavy ions in the LHC is under investigation [112]. A cooling system with a bandwidth of 5–20 GHz would require 12–15 m of longitudinal space per plane and beam, with pick-ups placed approximately 3/8 of the circumference away from the kicker. As in RHIC, the kickers would need to open to provide sufficient aperture for injection and ramping, and then close down on the beams at collision energy. Unlike in RHIC, they would also need to be compatible with the very high current proton beams in their open position. This is a very demanding requirement and would probably require a mechanical design that replaces the kicker tanks with smooth beam pipes during proton operation.

At collision energy in the LHC, IBS is not a strong effect and the role of the cooling system is, rather to extract more luminosity in a short time, from beams of rapidly diminishing intensity by drastically shrinking their emittances. Stochastic cooling could reduce the emittances by an

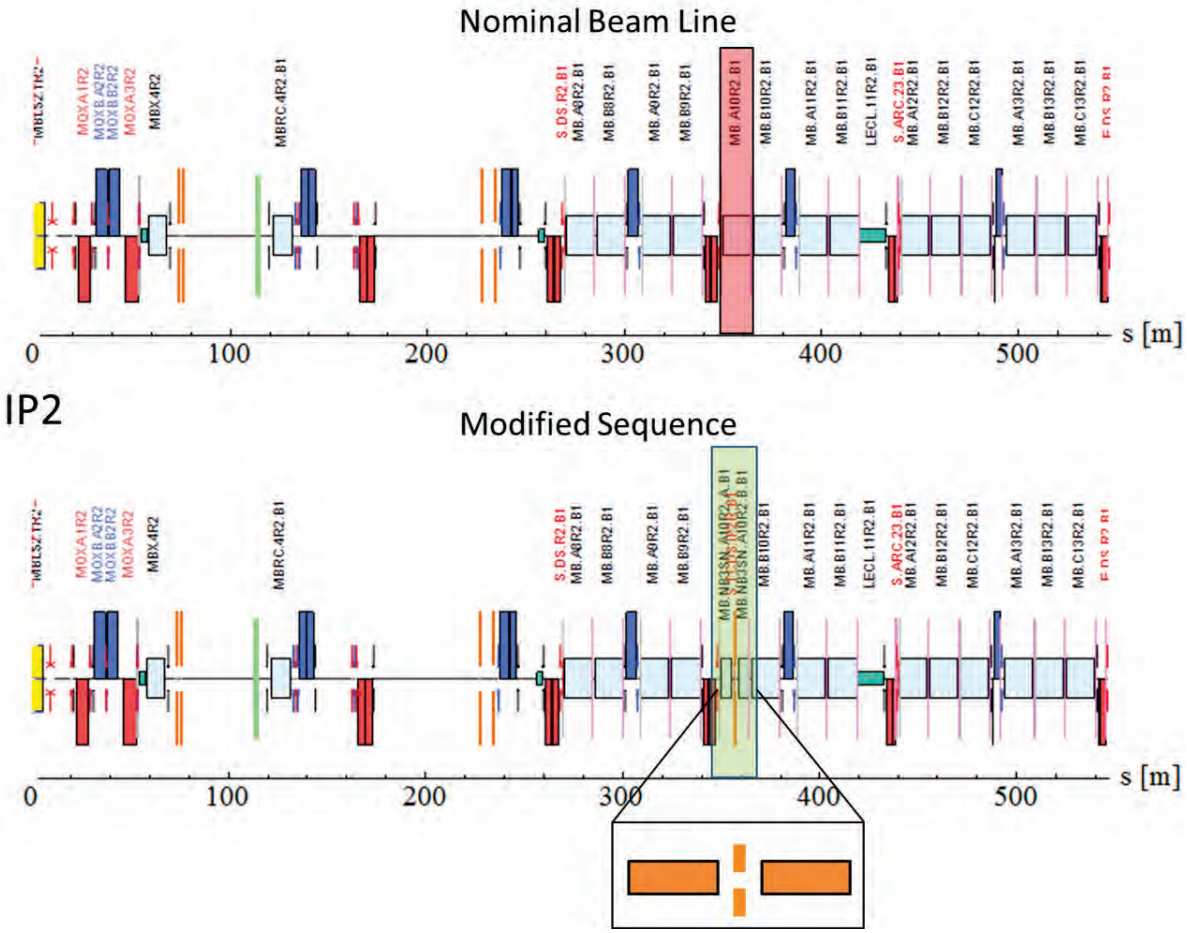

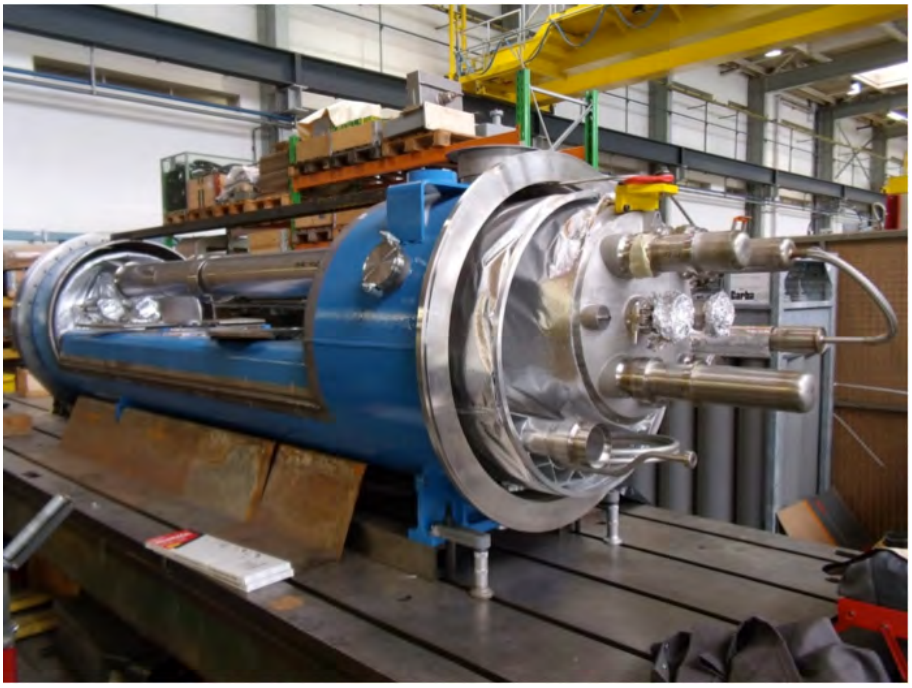

Fig. 27: Layout of the planned LHC warm dispersion suppressor collimator between two high-field (11 T) dipoles (top), and prototype of the cryogenic bypass for the warm collimator (bottom) [111].

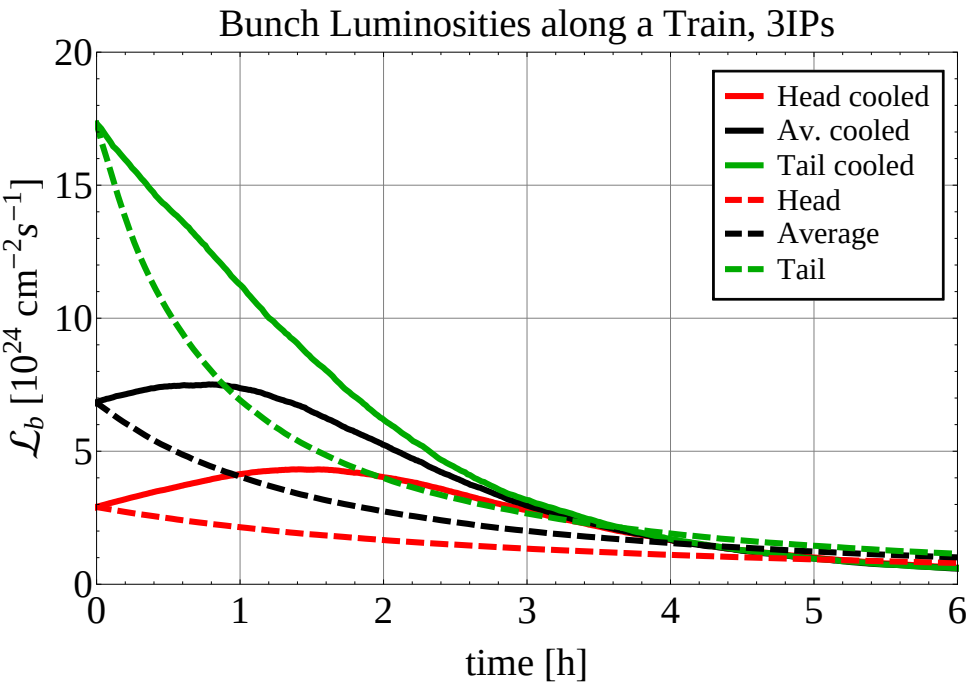

Fig. 28: Luminosity improvement from stochastic cooling in the LHC [112]. The three curves show the luminosity for bunches at the start middle and end of an SPS batch in the LHC, taking account of the variations in intensity and emittance along the batch (cf, Fig. 10).

order of magnitude, leading to the burn-off of around 90% of the initially injected ions. This would increase the average fill luminosity by 50% (Fig. 28) [112].

8 Future Ion Colliders

At the time of writing, preliminary considerations of hadron colliders beyond the LHC—looking two decades or more into the future—have begun in various parts of the world [113]. Among these is the so-called Future Circular Collider (FCC-hh), a hadron collider of 80-100 km circumference based on very high-field superconducting magnets, built as an extension of the CERN accelerator complex. The physics case for using such a machine for Pb+Pb and p+Pb collisions, as well as for p+p, is currently being articulated.

Taking for granted that the magnet technology to build such a collider will be developed, a first study of heavy-ion operation [114] assumes, for simplicity and definiteness, an injection scheme in which the LHC functions as the last injector synchrotron. It would be filled as for its own Pb+Pb operation and the beams then transferred to the FCC-hh at an intermediate point in the LHC ramp, filling only a fraction of its circumference (and hence limiting the number of locations for collisions).

At the energies envisaged, 20 TeV/nucleon for Pb (the equivalent of 50 TeV protons), synchrotron radiation damping is a very powerful beam-cooling mechanism. Transverse emittance damping times are less than 30 min. IBS growth rates are also much smaller than in the LHC, making for a remarkably efficient collider where the luminosity grows despite the rapid burn-off of the beam intensity. This is different from protons where the radiation damping needs to counter the beam-beam limit. Although radiation damping is even stronger in the longitudinal plane, RF noise is applied to maintain a constant bunch length and IBS only becomes significant when the emittance has shrunk by an order of magnitude.

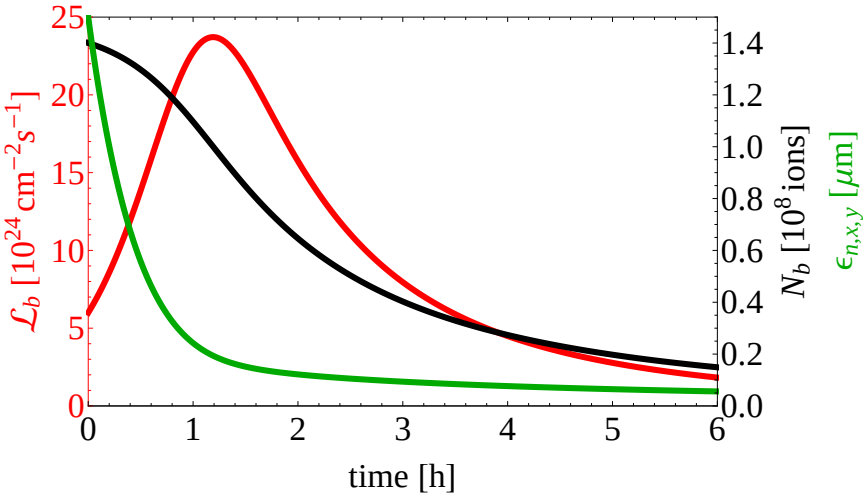

Fig. 29: Simulated evolution of beam intensity, emittance and luminosity of a single colliding Pb+Pb bunch pair in the FCC-hh envisaged at CERN (Courtesy M. Schaumann [114]).

Figure 29 shows the rapid emittance damping, intensity decay and luminosity growth and decay during an FCC fill for a single colliding bunch pair. With about 1000 bunches, the total luminosity would reach $10^{28}\,\mathrm{cm}^{-2}\mathrm{s}^{-1}$. Proton-lead collisions would exhibit a qualitatively similar luminosity evolution [114] with a peak luminosity exceeding $10^{30}\,\mathrm{cm}^{-2}\mathrm{s}^{-1}$, an order of magnitude higher than in the LHC. After a few hours, the beam is exhausted but meanwhile there has been time to prepare the next fill from the LHC, which, depending on the extraction and injection kickers, can be rapidly injected in a single or a few pulses.

9 SUMMARY

Ion colliders are built to study the interactions of quarks and gluons at high collision energies where a new form or matter is created, the Quark-Gluon-Plasma (QGP). The most important design considerations for ion colliders are the energy reach and range, the luminosity, and flexibility in changing species combinations and energies. Asymmetric species combinations are an essential part of the physics program. These requirements distinguish them from earlier colliders designed only for elementary particle physics.

The preparation of intense ion beams requires a successive increase in the ion charge state Z due to space charge, intrabeam scattering, charge change, and dynamic vacuum effects. The main luminosity limitations in a collider are the bunch intensity available from the injector, intrabeam scattering (RHIC) and the uncontrolled losses of secondary beams created in the collisions or from collimation (LHC).

RHIC is also the world's first and only collider of spin polarized beams, with a physics program aimed at disentangling the contributions of quarks, gluons and gluon orbital momentum to the proton spin.

Upgrades at RHIC and the LHC target higher luminosities and more flexibility. The primarily RHIC upgrades are the implementation of electron cooling to increase the luminosity at the lowest collision energies (below the nominal injection energy); source upgrades for more bunch intensity, and the full commissioning of at 56 MHz SRF cavity for more luminosity at the highest energies; and electron lenses for increased polarized proton luminosity. The main LHC upgrades specific to the heavy-ion program include increases in the bunch intensity and number of bunches from the injectors, upgrades to the collimation system, and possibly stochastic cooling during physics.

10 ACKNOWLEDGMENTS

The authors are thankful for discussions with many colleagues in particular J. Alessi, M. Bai, M. Blaskiewicz, A. Fedotov, M. Okamura, J.M. Brennan, D.J. Gardner, H. Huang, C. Montag, T. Roser, and P. Thieberger at BNL; R. Alemany, G. Arduini, P. Baudrenghien, T. Böhl, O. Brüning, R. Bruce, C. Carli, M. Giovannozzi, D. Kuchler, M. Lamont, D. Manglunki, S. Redaelli, G. Rumolo, M. Schaumann, K. Schindl, E. Shaposhnikova, R. Scrivens, J. Wenninger, and F. Zimmermann at CERN; R.W. Aßman at DESY; O. Boine-Frankenheim, K. Omet and P. Spiller at GSI; and R. Versteegen now at ESRF.

REFERENCES

[1] K. Johnsen, The ISR and accelerator physics, in *CERN 84-13* (1984).

[2] P. Asbo-Hansen, O. Barbalat, D. Boussard, M. Boutheon, J. Gareyte, H. Haseroth, J. Jamsek and S. Myers, Acceleration and stacking of deuterons in the CERN PS and ISR, *IEEE Trans. Nucl. Sci.* **24** (1977), pp. 1557-1560.

[3] M. Boutheon, R. Cappi, H. Haseroth, C.E. Hill, and J.-P. Koutchouk, Acceleration and stacking of alpha particles in the CERN Linac, PS and ISR, *IEEE Trans. Nucl. Sci.* **28** (1981), pp. 2049-2051.

[4] M. Harrison, T. Ludlam, S. Ozaki, RHIC project overview, *Nucl. Instrum. Methods A* **499** (2003), pp. 235-244.

[5] http://www.rhichome.bnl.gov/RHIC/Runs/

[6] O.S. Brüning and P. Collier and P. Lebrun and S. Myers and R. Ostojic and J. Poole and P. Proudlock (editors), LHC design report v.1: the LHC main ring, *CERN-2004-003-V1* (2004).

[7] O.S. Brüning and P. Collier and P. Lebrun and S. Myers and R. Ostojic and J. Poole and P. Proudlock (editors), LHC design report v.2: the LHC infrastructure and general services, *CERN-2004-003-V2* (2004).

[8] M. Benedict and P. Collier and V. Mertens and J. Poole and K. Schindl (editors), LHC design report v.3: the LHC injector chain, *CERN-2004-003-V3* (2004).

[9] L. Evans, The Large Hadron Collider from conception to commissioning: A personal recollection, *Reviews of Accel. Sci. and Technology* **3** (2010), pp. 261-280.

[10] B.V. Jacak and B. Müller, The exploration of hot nuclear matter, *Science* **337** (2012), pp. 310-314.

[11] N. Auerbach and S. Schlomo, η/S ratio in finite nuclei, *Phys. Rev. Lett.* **103**, 172501 (2009).

[12] The STAR Collaboration, The observation of an antimatter hypernucleus, *Science* **337** (2010), pp. 58-62.

[13] The STAR Collaboration, Observation of the antimatter helium-4 nucleus, *Nature* **473** (2011), pp. 353-35.

[14] STAR Collaboration, Studying the phase diagram of QCD matter at RHIC, *STAR White Paper* (28 March 2014).

[15] M. Schaumann and J.M. Jowett, Bunch-by-bunch analysis of the LHC heavy ion luminosity, *IPAC 2013, Shanghai* (2013), pp. 1391-1293.

[16] http://www.bnl.gov/rhic/physics.asp

[17] B. Müller, J. Schukraft, and B. Wyslouch, First Results from Pb+Pb collisions at the LHC, *Ann. Rev. Nucl. Part. Sci.*, **62** (2012), pp. 361-386.

[18] J. Schukraft, Heavy Ion Physics at the LHC: What's new? What's next? *Phys. Scr.*, **T158** 014003 (2013).

[19] A. Andronic, arxiv:1407.5003, to appear as an invited review in Int. J. Mod. Phys. A.

[20] S. Chatrchyan et al. (CMS collaboration), Observation and studies of jet quenching in PbPb collisions at nucleon-nucleon center-of-mass energy = 2.76 TeV *Phys.Rev.* **C84** 024906 (2011).

[21] G. Aad et al. (ATLAS Collaboration), Measurement of the Azimuthal Angle Dependence of Inclusive Jet Yields in Pb+Pb Collisions at $\sqrt{s_{\rm NN}} = 2.76\,\text{TeV}$ with the ATLAS Detector *Phys. Rev. Lett.* **111**, 152301 (2013).

[22] G. Aad, et al., ATLAS Collaboration, Measurement of Z Boson Production in Pb-Pb Collisions at $\sqrt{s_{NN}}$=2.76 TeV with the ATLAS Detector, *Phys. Rev. Lett.*, **110**, 022301, (2013).

[23] S. Chatrchyan et al. (CMS collaboration), Indications of suppression of excited Upsilon states in PbPb collisions at $\sqrt{s_{\rm NN}} = 2.76\,\text{TeV}$ *Phys.Rev.Lett.* , **107** 052302 (2011).

[24] K. Safarik, Overview of recent ALICE results, *Nucl. Phys. A*, **904-905** (2013), pp. 27c-34c.

[25] M. Wilde et al., Measurement of direct photons in pp and Pb-Pb collisions with ALICE, *Nucl. Phys. A* **904-905** (2013), pp. 573c–576c.

[26] B. Dönigus, (Anti-)matter and hyper-matter production at the LHC with ALICE, *Nucl. Phys. A*, **904-905** (2013), pp. 547c-550c.

[27] C.A. Salgado, J. Alvarez-Muniz, F. Arleo, N. Armesto, M. Botje, et al., Proton-nucleus collisions at the LHC: scientific opportunities and requirements, *J. Phys.* **G39**, 015010 (2012).

[28] B. Abelev, B. et al, Transverse Momentum Distribution and Nuclear Modification Factor of Charged Particles in p+Pb Collisions at $\sqrt{s_{NN}}$=5.02 TeV, Phys. Rev. Lett., **110**, 082302, (2013).

[29] V. Khachatryan et al., Observation of long-range, near-side angular correlations in proton-proton collisions at the LHC, *JHEP* **09**, pp. 1–37 (2010)

[30] S. Chatrchyan et al., Observation of long-range, near-side angular correlations in pPb collisions at the LHC. *Physics Letters B*, **718(3)** (2013), pp. 795-814.

[31] I. Alekseev et al., Polarized proton collider at RHIC, *Nucl. Instrum. Methods A* **499** (2003), pp. 392-414.

[32] E. Aschenauer, The RHIC spin program – achievements and future opportunities, *Fall Meeting of the Division of Nuclear Physics of the American Physical Society, Newport Beach* (2012).

[33] D. de Florian, R. Sassot, M. Stratmann, and W. Vogelsang, Evidence for polarization of gluons in the proton, *Phys. Rev. Lett.* **113**, 012001 (2014)

[34] M. Furman, Luminosity, in A.W. Chao, K.H. Mess, M. Tigner, and F. Zimmermann (eds.), *Handbook of accelerator physics and engineering*, 2nd edn. (World Scientific, 2013), pp. 311-318.

[35] M. Schaumann, Semi-empirical model for optimising future heavy-ion luminosity of the LHC, *IPAC 2014, Dresden* (2014), pp. 1033-1035.

[36] A.W. Chao, *Physics of collective beam instabilities in high energy accelerators*, (John Wiley, 1993).

[37] V. Lebedev, Intrabeam scattering, in A.W. Chao, K.H. Mess, M. Tigner, and F. Zimmermann (eds.), *Handbook of accelerator physics and engineering*, 2nd edn. (World Scientific, 2013).

[38] V.P. Shevelko, I.Yu. Tolstikhina, and Th. Stölker, Stripping of fast heavy low-charged ions in gaseous targets, *Nucl. Instrum. Methods B* **184** (2001), pp. 295-308.

[39] G. Weber et al., Beam lifetimes and ionization cross sections of U^{28+}, *Phys. Rev. ST Accel. Beams* **12**, 084201 (2009).

[40] W. Fischer et al., Injection and acceleration of Au^{31+} in the BNL AGS, *EPAC 2008, Genoa* (2008), pp. 313-315.

[41] C.J. Gardner (private communication 2014).

[42] D. Manglunki et al., The first LHC p-Pb run: performance of the heavy ion production complex, *IPAC 2013, Shanghai* (2014), pp. 2648-2650.

[43] E. Mahner, Review of heavy-ion induced desorption studies for particle accelerators, *Phys. Rev. ST Accel. Beams* **11**, 104801 (2008).

[44] M. Furman, Electron-cloud effect, in A.W. Chao, K.H. Mess, M. Tigner, and F. Zimmermann (eds.), *Handbook of accelerator physics and engineering*, 2nd edn. (World Scientific, 2013), pp. 163-167.

[45] W. Fischer, M. Blaskiewicz, J. M. Brennan, H. Huang, H. C. Hseuh, V. Ptitsyn, T. Roser, P. Thieberger, D. Trbojevic, J. Wei, S. Y. Zhang, and U. Iriso, Electron cloud observations and cures in the Relativistic Heavy Ion Collider, *Phys. Rev. ST Accel. Beams* **11**, 041002 (2008).

[46] P. Thieberger and M. McKeon and H.E. Wagner, Test for pulsed high current heavy ion synchrotron injection with an MP-Tandem Van de Graaf, *IEEE Trans. Nucl. Sci.*, NS-30, No 4 (1983), pp. 2746-2748.

[47] J.G. Alessi et al., Performance of the new EBIS preinjector, *PAC 2011, New York* (2011), pp. 1966-1968.

[48] T. Kanesue et al., The commissioning of the laser ion source for RHIC EBIS, *IPAC 2014, Dresden* (2014), pp. 1890-1892.

[49] P. Thieberger et al., Improved gold ion stripping at 0.1 and 10 GeV/nucleon for the Relativistic Heavy Ion Collider, *Phys. Rev. ST Accel. Beams* **11**, 011001 (2008).

[50] M.E. Angoletta, P. Baudrenghien, G. Bellodi, A. Blas, T. Bohl, et al. Ions for LHC: Performance of the Injector Chain, *IPAC 2011, San Sebastian* (2011), pp. 2529-2531.

[51] D. Manglunki, H. Bartosik, Y. Papaphilippou, M.E. Angoletta, G. Bellodi, A. Blas, et al, Performance of the CERN Heavy Ion Production Complex, *IPAC 2012, New Orleans* (2012), pp. 3752-3754.

[52] M. Chanel, LEIR: the Low Energy Ion Ring at CERN, *Nucl. Instrum. Methods A* **532** (2014), pp. 137-143.

[53] H. Burkhardt and D. Manglunki and M. Martini and F. Roncarolo, Investigation of space charge effects and intrabeam scattering for lead ions in the SPS, *EPAC 2004, Luzerne* (2004), pp. 1846-1848.

[54] D. Boussard, J.M. Brennan, T. Linnecar, Non-integer harmonic acceleration of lead ions in the CERN SPS, *PAC 1995, Dallas* (1995), pp. 1506-1508.

[55] J. M. Jowett and C. Carli. The LHC as a proton-nucleus collider, *EPAC 2006*, Edinburgh, pp. 550–552.

[56] J.M. Jowett, R. Alemany-Fernandez, P. Baudrenghien, D. Jacquet, M. Lamont, D. Manglunki, S. Redaelli, M. Sapinski, M. Schaumann, M. Solfaroli Camillocci, R. Tomas, J. Uythoven, D. Valuch, R. Versteegen, and J. Wenninger, Proton-nucleus collisions in the LHC, *IPAC 2013, Shanghai* (2013), pp. 49-51.

[57] U. Iriso and W. Fischer, Electron induced molecular desorption from electron clouds at the Relativistic Heavy Ion Collider, *Phys. Rev. ST Accel. Beams* **8**, 113201 (2005); Erratum, *Phys. Rev. ST Accel. Beams* **9**, 029901 (2006).

[58] W. Fischer, U. Iriso, and E. Mustafin, Electron cloud driven vacuum instability, *AIP Conference Proceedings* **773** (2004); BNL-73262-2004-AB, BNL C-A/AP/173 (2004).

[59] M. Blaskiewicz et al., Transverse instability in RHIC, *PAC 2003, Portland* (2003), pp. 3026-3028.

[60] C. Montag, J. Kewisch, D. Trbojevic and F. Schmidt Overcoming a fast transverse instability by means of octupole-induced tune spread in the Relativistic Heavy Ion Collider, *Phys. Rev. ST Accel. Beams* **5**, 084401 (2002).

[61] T. Satogata et al., Commissioning of RHIC deuteron-gold collisions, *PAC 2003, Portland* (2003), pp. 1706-1708.

[62] W. Fischer, P. Cameron, S. Peggs and T. Satogata, Tune modulation from beam-beam interaction and unequal radio frequencies in RHIC, *AIP Conference Proceedings* **693** (2003), pp. 252-255.

[63] J. Jowett, G. Arduini, R. Assmann, P. Baudrenghien, C. Carli, et al., First Run of the LHC as a Heavy-ion Collider, *IPAC 2011, San Sebastian* (2011), pp. 1837-1839.

[64] A. Hofmann, *The physics of synchrotron radiation*, Cambridge monographs on particle physics, nuclear physics, and cosmology, (Cambridge Univ. Press, Cambridge, 2004).

[65] J. M. Jowett, R. Alemany-Fernandez, R. Assmann, P. Baudrenghien, G. Bellodi, S. Hancock, M. Lamont, D. Manglunki, S. Redaelli, M. Sapinski, M. Schaumann, M. Solfaroli, R. Versteegen, J. Wenninger, and D. Wollmann, Heavy Ions in 2012 and the Programme up to 2022, *Proc. of the Chamonix 2012 Workshop on LHC Performance*, CERN-2012-006 (2012).

[66] R. Versteegen, R. Bruce, J.M. Jowett, M.J. McAteer, E.H. McLean, A.S. Langner, Y.I. Levinsen, T. Persson, S. Redaelli, B. Salvachua, P.K. Skowronski, M. Solfaroli Camillocci, R. Tomás, G. Valentino, J. Wenninger, and S.M. White. Operating the LHC Off-Momentum for p-Pb Collisions. *IPAC 2013, Shanghai* (2013), pp. 1439–1441.

[67] M. Blaskiewicz, J. M. Brennan, and K. Mernick, Three-dimensional stochastic cooling in the Relativistic Heavy Ion Collider, *Phys. Rev. Lett.* **105**, 094801 (2010).

[68] W. Fischer, A.J. Baltz, M. Blaskiewicz, D. Gassner, K.A. Drees, Y. Luo, M. Minty, P. Thieberger, and M. Wilinski, Measurement of the total cross section of uranium-uranium

collisions at $\sqrt{s_{\rm NN}} = 192.8$ GeV, *Phys. Rev. C* **89**, 014906 (2014).

[69] N.V. Mokhov and V.I. Balbekov, Beam and luminosity lifetime, in *Handbook of accelerator physics and engineering* 1st edn., (World Scientific, 1998).

[70] Y. Luo, W. Fischer, M. Blaskiewicz, J. M. Brennan, N. Kling, K. Mernick, and T. Roser, Burn-off dominated uranium and asymmetric copper-gold operation in RHIC, *Phys. Rev. ST Accel. Beams*, accepted for publication (23 July 2014).

[71] Y. Luo, W. Fischer, N.P. Abreu, A. Pikin, and G. Robert-Demolaize, Six-dimensional weak-strong simulation of head-on beam-beam compensation in the Relativistic Heavy Ion Collider, *Phys. Rev. ST Accel. Beams* **15**, 051004 (2012).

[72] J.M. Jowett, Parasitic beam-beam effects and separation schemes, in A.W. Chao, K.H. Mess, M. Tigner, and F. Zimmermann (eds.), *Handbook of accelerator physics and engineering*, 2nd edn. (World Scientific, 2013), pp. 311-318.

[73] H.-H. Braun, R.W. Assmann, A. Ferrari, J.-B. Jeanneret, J.M. Jowett, and I.A. Pshenichnov, Collimation of heavy ion beams in LHC, *EPAC 2004, Lucerne* (2004), pp. 551-553.

[74] H.H. Braun, A. Fassò, A. Ferrari, J.M. Jowett, P.R. Sala, and G.I. Smirnov, Hadronic and electromagnetic fragmentation of ultrarelativistic heavy ions at LHC, *Phys. Rev. ST Accel. Beams* **17**, 021006 (2014).

[75] G. Bellodi, R.W. Assmann, R. Bruce, M. Cauchi, J.M. Jowett, et al. First ion collimation commissioning results at the LHC. *IPAC 2011, San Sebastian* (2011), pp. 1813-1815.

[76] R. Bruce, R. W. Assmann, G. Bellodi, C. Bracco, H. H. Braun, S. Gilardoni, E. B. Holzer, J. M. Jowett, S. Redaelli, and T. Weiler. Measurements of heavy ion beam losses from collimation. *Phys. Rev. ST Accel. Beams* **12**, 011001 (2009).

[77] A.J. Baltz, M.J. Rhoades-Brown, and J. Weneser, Heavy ion partial beam lifetimes due to Coulomb induced processes, *Phys. Rev. E* **54** (1995), pp. 4233-4239.

[78] P. Grafström et al., Measurement of electromagnetic cross sections in heavy ion interactions and its consequences for luminosity lifetime in ion colliders, *PAC 1999, New York* (1999), pp. 1671-1673.

[79] Spencer R. Klein. Localized beam pipe heating due to e- capture and nuclear excitation in heavy ion colliders, *Nucl. Instrum. Methods A* **459** (2001), pp. 51-57.

[80] J.M. Jowett, J.B. Jeanneret, and K Schindl. Heavy Ion Beams in the LHC, *PAC 2003, Portland* (2003), pp. 1682-1684.

[81] J.M. Jowett, Hans-Heinrich Braun, M.I. Gresham, E. Mahner, A.N. Nicholson, et al. Limits to the performance of the LHC with ion beams. *EPAC 2004, Lucerne* (2004), pp. 578-580.

[82] R. Bruce, D. Bocian, S. Gilardoni, and J. M. Jowett, Beam losses from ultraperipheral nuclear collisions between $^{208}\mathrm{Pb}^{82+}$ ions in the large hadron collider and their alleviation, *Phys. Rev. ST Accel. Beams* **12**, 071002 (2009).

[83] S. Redaelli et al, Quench tests at the Large Hadron Collider with collimation losses at 3.5 Z TeV, *Proc. HB2012 Workshop, Beijing, China*, pp. 157–161, 2012.

[84] R. Bruce, J.M. Jowett, S. Gilardoni, A. Drees, W. Fischer, S. Tepikian, and S.R. Klein, Observations of beam losses due to bound-free pair production in a heavy ion collider, *Phys. Rev. Lett.* **99**, 144801 (2007).

[85] R. Bruce, J. M. Jowett, M. Blaskiewicz, and W. Fischer. Time evolution of the luminosity of colliding heavy-ion beams in BNL Relativistic Heavy Ion Collider and CERN Large

Hadron Collider. *Phys. Rev. ST Accel. Beams*, **13**, 091001, (2010).

[86] M. Bai et al., *Phys. Rev. Lett.* **96**, 174801 (2006).

[87] I. Alekseev et al., Configuration manual polarized proton collider at RHIC, BNL-97226-2006-IR, C-A/AP/455 (2012).

[88] W. Fischer and A. Bazilevsky, Impact of three-dimensional polarization profiles on spin-dependent measurements in colliding beam experiments, *Phys. Rev. ST Accel. Beams* **15**, 041001 (2012).

[89] A. Zelenski, G. Atoian, J.M. Fite, D. Raparia, J. Ritter, D. Steski, V.I. Davydenko, A.A. Ivanov, A. Kolmogorov, The RHIC polarized source upgrade, *PAC 2013, Pasadena* (2013), pp. 49-51.

[90] P.G. Sona, A new method proposed to increase polarization in polarized ion sources of H^- and D^-, *Energia nucleare*, Vol. 14, no. **5** (1967), pp. 295-299.

[91] S.Y. Lee, *Spin dynamics and snakes in synchrotrons*, (World Scientific, 1997).

[92] H. Huang, et al., Overcoming horizontal depolarizing resonances with multiple tune jumps, *Phys. Rev. ST Accel. Beams.* **17**, 081001 (2014).

[93] A. Bazilevski et al., Precision measurements of the proton beam absolute polarization with RHIC polarimeters, *AIP Conf. Proc.* **1149** (2008), pp. 723-726.

[94] H. Huang et al., Commissioning CNI proton polarimeters in RHIC, *EPAC 2012, Paris* (2002), pp. 338-340.

[95] M. Minty et al., Simultaneous orbit, tune, coupling, and chromaticity feedback at RHIC, *PAC 2011, New York* (2011), pp. 1394-1398.

[96] V. Ptitsyn et al., High luminosity electron-hadron collider eRHIC, *PAC 2011, New York* (2011), pp. 693-695.

[97] D. Trbojevic et al., NS-FFAG for electron-ion collider in RHIC (eRHIC), *PAC 2013, Pasadena*, (2013), pp. 553-555.

[98] J. L. Abelleira Fernandez et al., A Large Hadron electron Collider at CERN: report on the physics and design concepts for machine and detector. *J. Phys. G* **39**, 0750,01 (2012).

[99] I. Ben-Zvi and V. Ptitsyn, Electron-Proton and Electron-Ion Colliders, *Reviews of Accel. Sci. and Technology*, Vol. **7** (2014), this volume.

[100] A. Fedotov and I. Ben-Zvi, Beam dynamics and expected RHIC performance with 56 MHz RF upgrade, *PAC 2009, Vancouver* (2009), pp. 2483-2485.

[101] S. Nagaitsev et al., Experimental demonstration of relativistic electron cooling, *Phys. Rev. Lett.* **96**, 044801 (2006).

[102] A. Fedotov et al., Bunched beam electron cooler for low energy RHIC operation, *PAC 2013, Pasadena* (2013), pp. 363-365.

[103] V. Shiltsev, Y. Alexahin, K. Bishofberger, V. Kamerdzhiev, G. Kuznetsov, and X.-L. Zhang, Experimental demonstration of colliding-beam-lifetime improvement by electron lenses, *Phys. Rev. Lett.* **99**, 244801 (2007).

[104] W. Fischer et al., Status of head-on beam-beam compensation in RHIC, *ICFA Mini-Workshop on Beam-Beam Effects in Hadron Colliders (BB2013), CERN, CERN-2014-004* (2014).

[105] W. Fischer et al., First experience with electron lenses for beam-beam compensation in RHIC, *IPAC 2014, Dresden* (2014), pp. 913-917.

[106] R. Milner, Development of a polarized ^{3}He ion source for RHIC, *White paper* (2010),

http://cepstein.scripts.mit.edu/he3/wp-content/uploads/2011/06/He3_WhitePaper.pdf.

[107] J.D. Maxwell, Development of a polarized ^{3}He ion source for RHIC, *PoS (PSTP2013)* **047** (2013).

[108] M. Bai, E.D. Courant, W. Fischer, V. Ptitsyn, and T. Roser, Explore the possibility of accelerating polarized He-3 beams in RHIC, *IPAC 2012, Louisiana* (2012), pp. 172-174.

[109] L. Rossi, LHC Upgrade Plans: options and strategy, *IPAC 2011, San Sebastian* (2011), pp. 908–912.

[110] M. Karppinen et al., Status of 11 T Nb3Sn Dipole Project for the LHC, *Applied Superconductivity Conf. Charlotte* (2014).

[111] S. Redaelli, J.M. Jowett et al., LHC Collimation Review 2013, https://indico.cern.ch/event/251588/ (2013).

[112] M. Schaumann et al., Potential of stochastic cooling of heavy ions in the LHC, *IPAC 2014, Dresden* (2014), pp. 76-78.

[113] M. Benedikt, D. Schulte, J. Wenninger, and F. Zimmermann, Challenges for highest energy circular colliders, *IPAC 2014, Dresden* (2014), pp. 1-6; CERN-ACC-2014-0153 (2014).

[114] M. Schaumann, Heavy Ions in the FCC-hh, CERN Report and University of Aachen thesis, to be published (2014).